PHYSICAL REVIEW B VOLUME 51, NUMBER 22 1 JUNE 1995-II

Defect structure of ferrous oxide $Fe_{1-x}O$

W. Schweika

Institut für Festkörperforschung, Forschungszentrum Jülich, D-52425 Jülich, Germany

A. Hoser and M. Martin*

Institut für Physikalische Chemie und Elektrochemie, Universität Hanover, Callinstr. 3-3a, D-30167 Hanover, Germany

A. E. Carlsson

Department of Physics, Washington University, St. Louis, Missouri 63130

(Received 21 November 1994)

We have investigated the defect structure of nonstoichiometric wüstite $Fe_{1-x}O$ as a function of temperature and oxygen partial pressure by means of diffuse elastic neutron scattering of a single crystal at thermal equilibrium. Particularly for $T = 1423$ K and $x = 0.08$, a Fourier analysis yielded short-range order and lattice displacement parameters as well as the ratio of the numbers of vacancies to interstitials, $\rho = 4.0 \pm 0.5$. The measured short-range order showing a strong correlation between nearest interstitials and vacancies was simulated in a computer model. A further analysis yielded the size distribution of the vacancy-interstitial defect clusters exhibiting a large fraction of 30% of free vacancies, while a further 15% of the defects are bound in isolated so-called 4:1 defect clusters. The entire long-range displacement fields were modeled in a Kanzaki force approach using independent phonon data. Within the usual approach of a single-defect approximation the observed asymmetries of the diffuse scattering around the Bragg peaks were described by using Coulomb-like forces around the cation vacancies of random 4:1 defect clusters. The measured decrease of Huang scattering and the development of diffuse peaks with increasing nonstoichiometry was reproduced by a more general type of Kanzaki model for concentrated solid solutions. Therefore, we used the same defect model of the 4:1 cluster, although surrounded with two occupied cation shells to screen the long-range displacement fields.

I. INTRODUCTION

The iron oxide wüstite, $Fe_{1-x}O$, exhibits an extremely large deviation from stoichiometry, x, which extends from 5% up to 15% as shown the phase diagram[1] (cf. Fig. 1). The nonstoichiometry, x, is due to an oxidation of divalent iron to trivalent iron. It can be adjusted by temperature, T, and oxygen partial pressure, p_{O_2}.[2] In comparison to other transition metal oxides, such as $Ni_{1-x}O$, $Co_{1-x}O$, or $Mn_{1-x}O$, which also crystallize in the NaCl structure and where x is very small ($x < 10^{-4}$) at low oxygen partial pressures, wüstite exhibits a minimal cation deficit of about 5% even at the lowest possible oxygen partial pressures in equilibrium with metallic iron. At high oxygen activities, where x may reach 15%, the neighboring phase of wüstite is magnetite, Fe_3O_4 (cf. Fig. 1). It crystallizes in the spinel structure, where the oxygen ions form again a fcc sublattice, while the iron ions, Fe^{2+} and Fe^{3+}, now occupy both the octahedral and the tetrahedral sublattices. Because of the large values of x and the similarity of the structures, there have been several attempts to explain the defect structure of wüstite by defect aggregates which are precursors of the spinel structure. The simplest subunit in this sense would be a cluster formed by a trivalent iron ion in the interstitial (tetrahedral) sublattice of wüstite and four neighboring cation vacancies (occupying octahedral sites

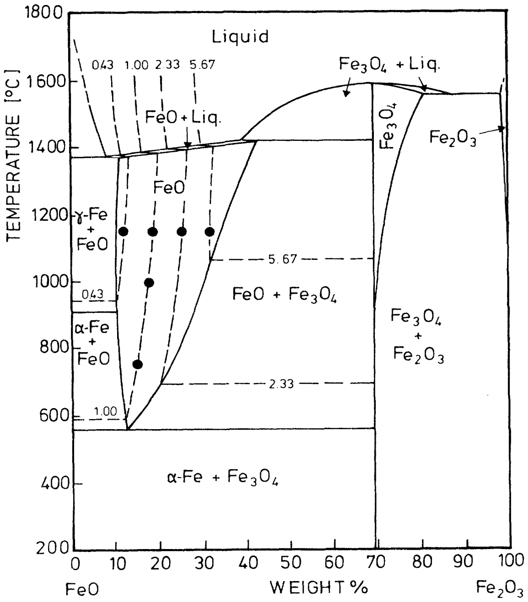

FIG. 1. Phase diagram of iron-oxygen after Muan and Osborn. Investigated states of the present study are indicated (dots) in the wüstite phase field. Dashed lines denote the ratios of the CO_2/CO atmospheres, which can be used to achieve the equilibrium conditions.

0163-1829/95/51(22)/15771(18)/$06.00 51 15 771

in the regular cation sublattice). This so-called 4:1 cluster (cf. Fig. 2) possesses five negative charges relative to the ideal lattice. Larger *m:n* clusters composed of *m* vacancies and *n* interstitials can be formed according to the same building principle combining several 4:1 clusters, either edge, corner, or face sharing. In addition the charge state of the clusters might change by binding electron holes, yielding clusters with negative effective charges between 0 and 5. On the other hand, defects in the oxygen sublattice are more unlikely than defects in the cation sublattices because of the large size of the oxygen ions compared with the iron ions. Indirectly this is reflected by the very small diffusion coefficient of oxygen[3] compared to that of iron.[4] This picture of the defect structure of wüstite is confirmed by theoretical calculations of the formation energies of clusters in transition metal oxides.[5–7] Particularly in wüstite, they yield high binding energies of the 4:1 clusters, which stabilize them even at elevated temperatures. The results of the first neutron diffraction study of wüstite by Roth[8] were already interpreted in terms of clustering of defects. Since then, wüstite has been regarded as the prototype of a strongly disordered crystalline compound containing defect clusters. One should perhaps note that the term clustering commonly used in this context could be misleading, since the correlation between cation vacancies and interstitials can in fact be understood as an ordering tendency and in this case presumably towards the neighbored spinel phase.

However, the exact defect structure, i.e., the defect configuration and the associated displacement fields around the defects, is still under discussion, despite the numerous experimental investigations. These can be divided into two classes: In structural investigations, x-ray,[9–11] neutron,[8,12–15] and electron,[16–18] diffraction and scattering methods as well as Mössbauer[19] and perturbed angular correlation (PAC) spectroscopy[20] were used to study polycrystalline and single-crystalline samples. As a result of these studies clusters of different size and composition were proposed, ranging from the 2:1 Roth clusters and 4:1 clusters, to 13:4 clusters or even larger aggregates. A compilation of all proposed cluster types can be found in Ref. 21. However, many of these structural studies were done on quenched samples, which raises doubts as to whether the defect structure at high temperatures has really been observed. Due to the very short relaxation times of defect equilibria at high temperatures, it seems more probable that a defect structure frozen-in at intermediate temperatures has been seen in these experiments. The results of these studies become even more questionable when one notes that the wüstite phase is thermodynamically stable only at temperatures above 570 °C and oxygen partial pressures $-26 < \log_{10} p_{O_2} < -6$ (p_{O_2} in bar).[2] Below this temperature wüstite decomposes into iron and magnetite. This means that iron and spinel Fe_3O_4 precipitations could affect experiments on quenched samples. From *in situ* Rietveld experiments[15] occupation numbers for regular and interstitial lattice sites were obtained from which the ratio of vacancy and interstitial concentrations, $\rho = [V]/[FeI]$, can be calculated. For one composition, x=0.08, the authors report with increasing temperature, $850 < T < 1100\,°C$, increasing ρ values, $2.6 < \rho < 4.3$, which they interpret by a transition from large clusters at low temperatures to smaller clusters and free vacancies at high temperatures. Diffuse scattering experiments offer a direct approach to the local order. Koch and Cohen[9] proposed on the basis of such measurements on quenched samples a 13:4 cluster, which is formed by 4:1 subunits, to be a typical element of the defect structure. In particular one diffuse x-ray experiment was carried out under *in situ* conditions.[11] It was concluded from this measurement that the typical cluster should consist of two incomplete corner-sharing 4:1 clusters aligned along ⟨110⟩ directions. In contrast to these structural investigations thermodynamic and transport measurements were performed to obtain the nonstoichiometry,[22] tracer-diffusion coefficients,[3,4,23] the chemical diffusion coefficient,[24] the electrical conductivity,[25,26] and creep data[27] as function of T and p_{O_2}. These data can be obtained under *in situ* conditions and were used to model the defect structure of wüstite and to test proposed cluster models.[28,29,21] However, again a wide spectrum of clusters ranging from 4:1 to 13:4 clusters, sometimes with a periodic spacing, was deduced from the macroscopic observations. Guided by superstructure peaks in TEM studies on quenched and annealed samples, new phases, P' and P'', were also proposed and their possible existence at high temperatures was discussed.[16–18]

The above discussion shows the need for an extensive structural study of wüstite under *in situ* conditions covering several temperatures and compositions and yielding sufficient information for a sound structure determination. Therefore we have performed *in situ* diffuse elastic neutron scattering experiments, the results of which we

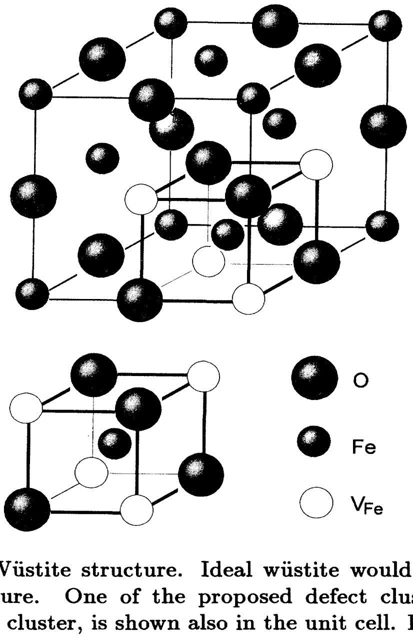

FIG. 2. Wüstite structure. Ideal wüstite would have the NaCl structure. One of the proposed defect clusters, the so-called 4:1 cluster, is shown also in the unit cell. It consists of a tetrahedral cation surrounded by four nearest cation vacancies. This 4:1 defect cluster is expected to have the charge 5−, since there are four O^{2-} and one Fe^{3+} interstitials.

have analyzed using different types of data analysis to deduce the defect structure under equilibrium conditions. The remainder of the paper is organized as follows: in Sec. II we describe the experimental procedure and the results, part of which has been published before.[30] In Sec. III one particular data set is used for a Fourier analysis, from which occupation numbers in the different sublattices and short-range-order parameters can be obtained. On the basis of these results, Sec. IV introduces a simple defect model which uses the Kanzaki-force approach to calculate the displacement fields around the defects and describes the experimental results well. In Sec. V the results and possible implications are discussed.

II. EXPERIMENTAL METHOD AND MEASURED DIFFUSE INTENSITIES

A. Samples and environment

Two single-crystalline samples were prepared from iron Fe and hematite Fe_2O_3 (purity of the samples 0.999 99) under 2×10^{-8} mbar oxygen partial pressure in a cold levitation crucible by the Czochralski method.[30] Large specimens of good quality were grown along a $\langle 100 \rangle$ direction up to a size of about $10 \times 10 \times 40$ mm^3. The mosaicity was found to be better than 2° FWHM, being sufficient for the diffuse-scattering experiments.

The samples were spark cut and further cut by a diamond saw in order to facilitate mounting the specimens with either the (100) or (110) planes horizontal on an Al_2O_3 sample holder. Thin platinum spacers were used to avoid direct contact in order to prevent any chemical reaction or interdiffusion of the two oxides.

We used a special furnace,[31] in which the defined oxygen partial pressure was achieved by a constant flow (37 l/h) of a CO/CO_2 gas mixture of fixed ratio and at normal pressure through the sample chamber. Various gas mixtures were produced by the gas mixing pumps which enabled us to change the oxygen partial pressure at ambient temperatures[32] determining the deviations from stoichiometry, x, of the $Fe_{1-x}O$ sample at high temperatures. The relaxation times for equilibrating the sample after changing the flow gas mixtures were in the order of 1 h at 1423 K. These times are determined by the time to establish the new gas mixtures in the furnace volume as well as by the diffusion properties of the sample. The change in x means that the single crystal has to grow or to shrink (up to 9% in volume) by exchange of oxygen with the gaseous phase and diffusion of the cations. In a similar study[33,31] on $Mn_{1-x}O$ the surface became porous because of this. Here, in the case of $Fe_{1-x}O$, however, the surface remains smooth. Temperatures were changed only slowly as required by the sensitive ceramic interior of the furnace. Heating and cooling at a rate of 200 K/h gave reproducible diffuse scattering results between 723 and 1423 K. The temperature was controlled by two thermocouples (PtRh6-PtRh30). The temperature gradient at the sample position was about 5 K/cm. The absolute accuracy of the measured temperature was estimated to ±10 K.

B. Diffuse neutron scattering experiments

The diffuse neutron scattering experiments were performed at the time-of-flight (TOF) spectrometer for diffuse scattering, DNS, in Jülich, using a wavelength of $\lambda = 3.3$ Å. By the TOF measurements the diffuse elastic signal can be easily distinguished from the high background due to inelastic scattering events. Typical time-of-flight spectra for $Fe_{1-x}O$ (x=0.08 and T=1423 K) and a particular sample orientation are given as examples in Fig. 3. The signals of interest, the elastic diffuse intensities, are centered at TOF channel 88. Most apparent for shorter times of flights, further neutrons were detected which have gained energy by inelastic, (multi-) phonon scattering but also by quasielastic paramagnetic scattering events. The broadening of the elastic intensity is in general fully described by the instrumental resolution. The elastic scattering at high scattering angles, Fig. 3(a), is low in this particular case and comparable to the weak background due to incoherent scattering of iron. At low scattering angles, Fig. 3(b), the elastic scattering intensity is typically also low. In addition, a broader additional air scattering becomes just noticeable by a line shape analysis around the elastic line. The strong elastic intensity [cf. Fig. 3(c)] corresponds to the most intense diffuse elastic peak. In most cases the energy resolution of 1 meV (FWHM) was sufficient to sep-

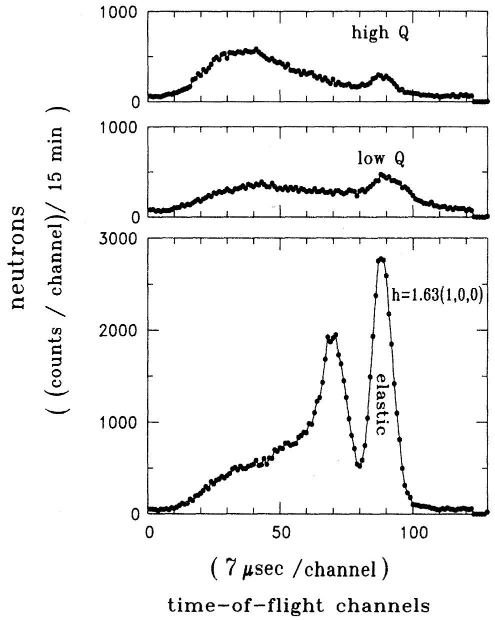

FIG. 3. Typical time-of-flight spectra as measured for $Fe_{0.92}O$ at T=1423 K for one sample orientation. The elastic scattering appears around channel 88. In addition a high inelastic scattering background, in particular in energy gain of the neutrons at shorter times, is seen due to (multi-) phonon scattering and paramagnetic scattering events. Examples show the variations of elastic scattering intensities, which may be small at high (top) as well as at low **Q** vectors (middle) in comparison to the maximum of the diffuse elastic intensity at $\mathbf{h} = (1.63, 0, 0)$ (bottom).

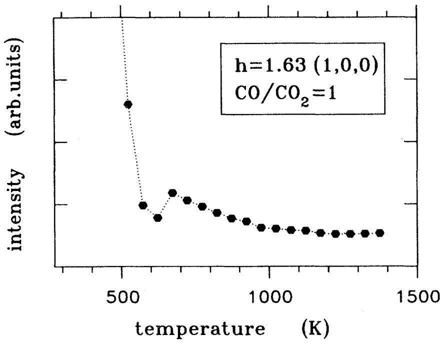

FIG. 4. Variation of the diffuse elastic peak intensity at $\mathbf{h} = (1.63, 0, 0)$ during heating in a CO/CO_2 atmoshere of ratio one. The discontinuity around 650 K indicates the phase transition from a metastable long-range-ordered wüstite to the homogeneous, however still metastable, disordered wüstite phase. At higher temperatures the intensity is steadily decreasing without any particular changes at the boundary to the stable wüstite phase field at 850 K and slightly rising again above 1300 K.

arate by fit procedures[34] the elastic scattering from the inelastic background. Furthermore, a few detectors were also affected by background contributions due to the furnace, i.e., the Debye-Scherrer rings of the PtRh heating element. The magnitude of this background scattering was determined by measurements of the empty furnace.

At each measured composition and temperature we rotated the sample in steps of 2.5° and collected simultaneously with 64 detectors the diffuse-scattering in a wide angle range (2° –132°). The measurements for one plane covered typically 3000 up to 5000 TOF spectra. Due to the high flux — the monochromatized beam was horizontally and vertically focused— such measurements took less than a day with generous counting statistics, i.e., in the order of 10 000 thousand counts of elastically scattered neutrons in the diffuse peaks. As usual the calibration was done using the incoherent scattering of vanadium as reference.

We measured the diffuse elastic intensities of wüstite single crystals at various temperatures and various deviations from stoichiometry. Two-dimensional data sets in a (100) plane in reciprocal space were measured both in the stability field of wüstite, at T = 1023, 1273, and 1423 K, using a CO/CO_2 ratio of one (which corresponds to nonstoichiometries x=0.063, 0.076, 0.079) and with samples slowly cooled to room temperature. At the highest temperature, T=1423 K, the study was extended to different deviations from stoichiometry achieved by various flow gas mixtures of CO/CO_2 (see Table I). At 1423 K with x=0.08 and at room temperature we also measured two-dimensional data in a (110) plane. During heating (e.g., Fig. 4) and cooling, and also during the changes

TABLE I. Measuring conditions of the $Fe_{1-x}O$ single crystal for the diffuse neutron scattering experiments. The deviation from stoichiometry x is determined by the temperature and the oxygen partial pressure achieved by CO_2/CO flow gas mixtures.

T (K)	CO_2/CO	p_{O_2} (Nm^{-2})	x
300	(air)		(0.06)
1023	1.00	1.9×10^{-15}	0.063(3)
1273	1.00	7.0×10^{-10}	0.076(3)
1423	0.43	3.4×10^{-8}	0.054(3)
1423	1.00	1.9×10^{-7}	0.079(3)
1423	2.33	1.0×10^{-6}	0.104(3)
1423	5.67	5.9×10^{-6}	0.131(3)

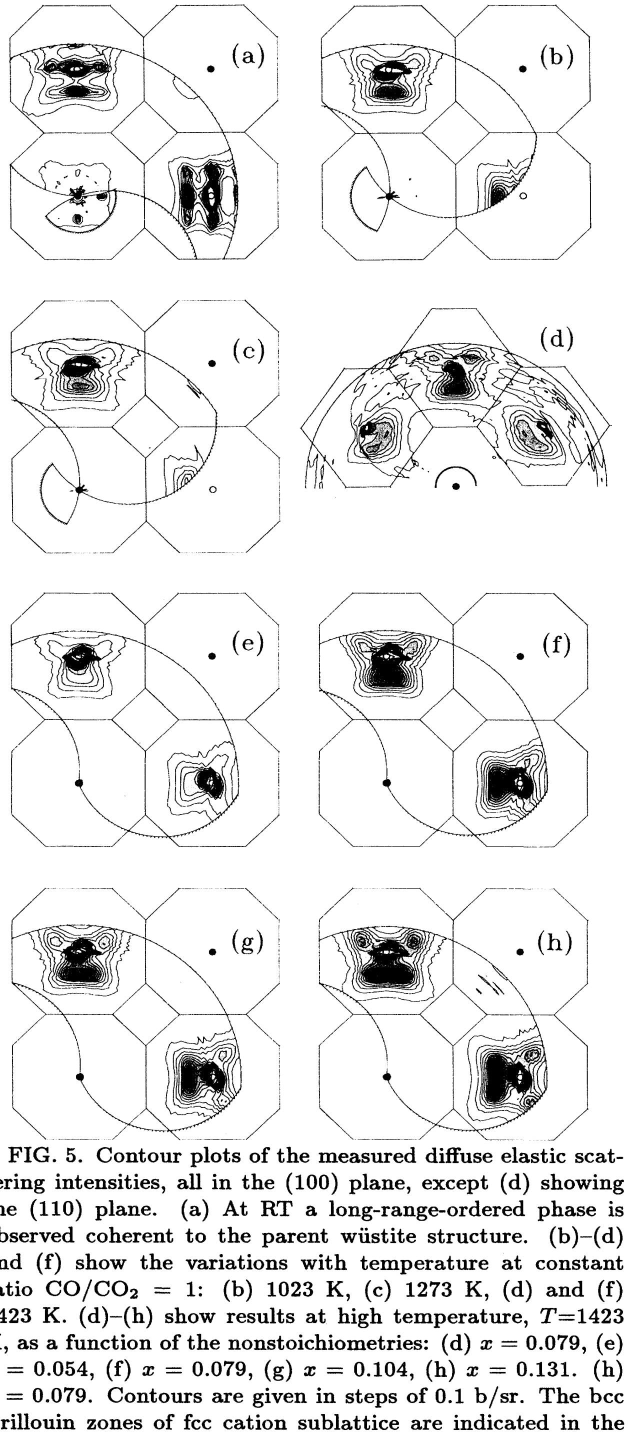

FIG. 5. Contour plots of the measured diffuse elastic scattering intensities, all in the (100) plane, except (d) showing the (110) plane. (a) At RT a long-range-ordered phase is observed coherent to the parent wüstite structure. (b)–(d) and (f) show the variations with temperature at constant ratio CO/CO_2 = 1: (b) 1023 K, (c) 1273 K, (d) and (f) 1423 K. (d)–(h) show results at high temperature, T=1423 K, as a function of the nonstoichiometries: (d) x = 0.079, (e) x = 0.054, (f) x = 0.079, (g) x = 0.104, (h) x = 0.131. (h) x = 0.079. Contours are given in steps of 0.1 b/sr. The bcc Brillouin zones of fcc cation sublattice are indicated in the figure.

of the oxygen partial pressure we measured the diffuse scattering also at the most intense diffuse peak.

C. Experimental results

After slow furnace cooling (≈ 200 K/h) of the specimen, but also just after the single-crystal growth, an incommensurate long-range-ordered phase was found with reciprocal cell vectors $\delta \approx 0.37(1,0,0)$ as shown in Fig. 5(a). In some cases additional peaks also occurred with $\delta \approx 0.37(1,1,0)$. These long-range-ordered, incommensurate phases (P' and P'') have been reported previously from x-ray scattering[9] and TEM studies.[17] (The latter found similar results for quenched samples and for samples annealed at 300 °C, because it was not possible to quench in the structure from 1000 °C. In addition the TEM images showed 110-Bragg peaks, referring to the FeO unit cell, which indicate a precipitation of the neighbored spinel phase Fe_3O_4.)

In order to explain the peak intensities measured by Koch and Cohen,[9] models of the superstructure were devised including not only occupational ordering of Fe vacancies and interstitials, but also displacive modulations.[9,35] Note that according to the phase diagram in Fig. 1 this long-range-ordered wüstite phase should be only metastable compared to a two phase mixture of iron and magnetite Fe_3O_4. However, within our experimental resolution our crystals show no indications of any iron or Fe_3O_4 precipitates. The diffuse scattering as a function of the scattering angle, including the peak at $\mathbf{h} \approx (1.63,0,0)$, was measured during heating (cf. Fig. 4) and cooling, and an order-disorder phase transition occurred around $T_0 = (623 \pm 50)$ K. While at higher temperatures the peak intensity increased with lowering the temperature, at T_0 a discontinuous transition occurred with a clear loss in the diffuse peak intensity. During further cooling the intensity increased again. No particular change of the diffuse scattering was found at the equilibrium phase boundaries at temperatures around 843 K.

The diffuse elastic scattering results for the high temperature measurements under equilibrium conditions are shown as contour plots in Figs. 5(b)–5(h). For all measurements at different points in the stable wüstite phase field, we found a pronounced diffuse scattering around the 200 Bragg peak. The two common features which evolve with increasing nonstoichiometry are first, a diffuse peak at $\mathbf{h} \approx (1.63,0,0)$ (the position of the superlattice spot at low temperatures) and second, two subsidiary peaks which appear at $\mathbf{h} \approx (2.2,\pm 0.4,0)$. Apparently, the defects in the equilibrium high-temperature phase produce a markedly, qualitative different scattering picture compared to the room temperature data. In comparison to the long-range-ordered phase no diffuse peaks were found at the other superlattice positions, which is contrary to the earlier expectations[36] resulting from x-ray measurements.[11] The first x-ray *in situ* measurements of Koch and Cohen[9] showing the raw data along a (100) direction are consistent with the observed asymmetry of the intensities at $\mathbf{h} = (2 \pm \delta, 0, 0)$ found here. With increasing deviation from stoichiometry, x, these diffuse peak intensities grow fairly linearly to x. However, looking closer to changes in the shape of the diffuse peak, one notices at lowest nonstoichiometry, $x = 0.054$, that the diffuse intensity around $\mathbf{h} \approx 0.82 \cdot (2,0,0)$ appears more like a shoulder, while with increasing concentration of defects the relative intensity maximum becomes more pronounced, and also extended perpendicular to the [100] axis. It is noteworthy that close to the Bragg peaks no significant indications of any Huang scattering can be seen, which are expected to be caused by long-range displacement fields of the defects.

TABLE II. Neutron scattering lengths, incoherent scattering, and thermal neutron absorption cross sections (Ref. 37).

	b 10^{-12} cm	$\sigma_{\rm inc}$ 10^{-24} cm^2	$\sigma_{\rm abs}$ 10^{-24} cm^2
Fe	0.9450(20)	0.40 (11)	2.56(3)
O	0.5803 (4)	0.00 (8)	0.00(2)
V	-	5.08 (6)	5.08(4)

In Fig. 5(d) the diffuse scattering in the (110) plane at 1423 K and $x = 0.08$, is shown. An additional diffuse peak was found at $\mathbf{h} \approx 0.82 \cdot (1,1,1)$. Together with the data of the (100) plane [cf. Fig. 5(f)] these were analyzed in terms of three-dimensional short-range order and displacement parameters, as it is discussed below. All neutron scattering properties required for the data analysis, such as the cross sections for the coherent and incoherent scattering and also for the absorption, were taken from the compilation of Sears[37] (see Table II).

Regarding the temperature dependence of the diffuse scattering in the (100) plane as measured for T =973, 1273, and 1423 K [see Figs. 5(b), 5(c), and 5(f)] at a constant ratio of $CO/CO_2 = 1$, which means also a similar nonstoichiometry x, one notices only a slight variation of the diffuse intensities.

The Brillouin zones of the fcc cation sublattice are also shown in Fig. 5. At least one point becomes immediately obvious: only short-range ordering of cation vacancies cannot explain the scattering pattern, since then one should observe exactly the translational symmetry properties of the Brillouin zones. Taking interstitials into regard as well, it is possible to explain parts of the differences for instance between the diffuse scattering around the origin and around the 200 Bragg peak. Furthermore, lattice displacements ought to be important to describe the asymmetry across the 200 Bragg peak, as it is discussed later.

III. ANALYSIS OF THE DEFECT STRUCTURE AND DISORDER IN $Fe_{0.92}O$ AT T=1423 K

A. Scattering formulation

In order to facilitate the interpretation of the diffuse-scattering data, we begin by describing the relationship between this scattering and the real-space structure of the material. The diffuse scattering of binary solid solutions on multiple sublattices has been treated by Hayakawa.[38] For the Fourier analysis described below we follow his approach closely. Here we give also a formulation as required for the Kanzaki model calculations presented in the next section, and give a brief discussion of various formulations used in the literature.

The diffuse scattering in $Fe_{1-x}O$ is likely due to the following defects, relative to the ideal NaCl structure, along with the correlations of these defects. We assume that the anion sublattice (fcc) is always completely filled by oxygen, $c^{\mathrm{O}}_{\mathrm{sub}} = 1$, and no interstitial oxygen exists, $c^{\mathrm{O}}_{\mathrm{int}} = 0$. The cation sublattice (fcc) may contain vacancies, with a concentration $c_{\mathrm{sub}} = c^{\mathrm{Fe}}_{\mathrm{sub}} = 1 - x\frac{\rho}{\rho-1} = 1 - c^{\mathrm{vac}}_{\mathrm{sub}}$, and iron ions may be found on the tetrahedral interstitial sites; $c_{\mathrm{int}} = c^{\mathrm{Fe}}_{\mathrm{int}} = \frac{1}{2}\frac{x}{\rho-1} = 1 - c^{\mathrm{vac}}_{\mathrm{int}}$, where $\rho = N_{\mathrm{vac}}/N_{\mathrm{int}}$ is the ratio of vacancies to interstitials. The tetrahedral interstitial sites form an *sc* sublattice, which has twice as many sites as the cation sublattice. For simplicity of notation, we find it convenient to separate the interstitial sublattice into two distinct fcc sublattices, identical to the cation sublattice. For this reason, the sums below over sublattices should be thought of as sums over three sublattices.

In order to describe the defect correlations, we introduce an occupation variable $c_s(\mathbf{R}) = 1$ or 0, if a lattice cell at the site R of the sublattice s is occupied by Fe or not. The correlations of the occupational fluctuations are defined by

$$g_{s,s'}(\mathbf{R} - \mathbf{R}') = \langle c_s(\mathbf{R}) c_{s'}(\mathbf{R}')\rangle - c_s c_{s'}. \tag{1}$$

The self-correlation function for $\mathbf{R} = \mathbf{R}'$ is

$$g_0 = \sum_s g_{s,s}(0) = c^{\mathrm{Fe}}_{\mathrm{sub}}(1 - c^{\mathrm{Fe}}_{\mathrm{sub}}) + 2c^{\mathrm{Fe}}_{\mathrm{int}}(1 - c^{\mathrm{Fe}}_{\mathrm{int}}). \tag{2}$$

We define the difference vector $\mathbf{R_m} = \mathbf{R} - \mathbf{R}'$. The Cowley-Warren[39] short-range-order parameters $\alpha_{\mathbf{m}}$ for binary solutions on one (sub-)lattice are then expressed by

$$\alpha^{(s,s)}_{\mathbf{m}} = g_{s,s}(\mathbf{R_m})/g_{s,s}(0). \tag{3}$$

We also use the indices lmn, $\mathbf{m} = (l, m, n)$, for convenience, where the length unit is $a/4$ and a is the lattice constant. It is further useful to distinguish three types of correlations (adopting the notation of Hayakawa *et al.*[38] and Gartstein *et al.*[11]): The first type {220}, for which all l, m, n are even and $\mathrm{Mod}(l + m + n, 4) = 0$. This condition applies to all site separations on the cation sublattice, and to some of the separations on the interstitial sublattice. The second type {200}, for which again all l, m, n are even but $\mathrm{Mod}(l + m + n, 4) \neq 0$. This applies to those separations on the interstitial sublattice which do not correspond to fcc lattice separations. The third type {111}, for which all l, m, n are odd. This condition applies to intersublattice correlations only. The resulting collection of separations has bcc symmetry properties. Because of the symmetry properties corresponding to these different types of correlations, it is possible to distinguish most but not all of them by a Fourier analysis of the diffuse scattering. In the following, we shall also use the indices in braces {220}, {200}, and {111}, respectively, in order to denote these three *types* of correlations. The Brillouin zones for these three types of correlations describe the translational symmetry properties of the short-range order are shown for the (100) plane in Fig. 6.

The total (elastic) differential scattering cross section per unit cell is written in the kinematic approximation as

$$\frac{d\sigma}{d\,\Omega}(\mathbf{Q}) = \frac{1}{N}\langle |A(\mathbf{Q})|^2\rangle, \tag{4}$$

where N is the number of unit cells in the system,

$$A(\mathbf{Q}) = \sum_{\mathbf{r}} \sum_i b^i(\mathbf{r}) e^{-W^i} e^{i\mathbf{Q}\cdot\mathbf{r}}, \tag{5}$$

W^i is the Debye-Waller factor, and $b^i(\mathbf{r})$ denotes the scattering amplitudes at the particle positions. For crystalline material it is convenient to use $c^i_s(\mathbf{R})$ if an atom of type i is in a unit cell around the mean lattice site $\mathbf{R}_s$, where s labels the sublattices. Since the atoms may be displaced from the mean lattice sites $\mathbf{R}$ we have $\mathbf{r}_s = \mathbf{R}_s + \mathbf{u}(\mathbf{R}_s)$. The elastic diffuse-scattering measurements, with an energy resolution of 1 meV, obtain a quasistatic picture of the short-range order and static lattice displacements (equivalent to x-ray diffraction), which is appropriate for the formalism described here. The phonon contributions were separated experimentally. Therefore thermal displacements are not treated here.

The diffuse-scattering amplitude, due to the disorder in the crystal, is obtained with respect to the scattering of the mean lattice:

$$A_d(\mathbf{Q}) = A(\mathbf{Q}) - \langle A(\mathbf{Q})\rangle. \tag{6}$$

However, in model calculations within the single defect approximation one typically refers to the ideal lattice instead. The Fourier analysis is based on a Tay-

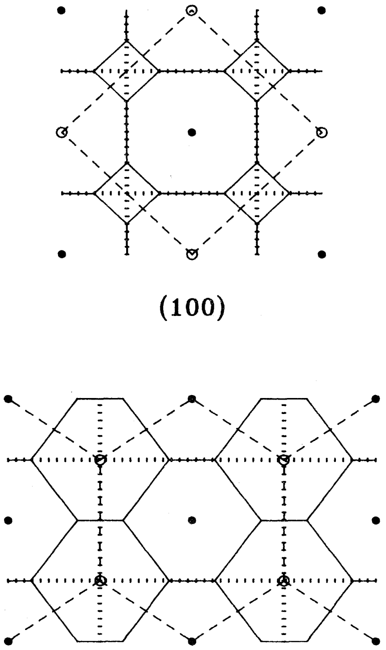
(100)

(110)

FIG. 6. Zone boundaries in the (100) and (110) planes for three types of correlations (i) on the fcc cation sublattice, (ii) on the sc interstitial sublattice of tetrahedral sites (dotted), (iii) between these two sublattices (dashed).

lor expansion of the phase factors [see Eq. (5)] assuming that $\mathbf{Q}\cdot\mathbf{u}(\mathbf{R}_s) \ll 1$. One then obtains for the diffuse-scattering cross section

$$\frac{d\sigma}{d\Omega}_d(\mathbf{Q}) = \frac{d\sigma}{d\Omega}_{\mathrm{Laue}} e^{-2W} \times \sum_{\mathbf{m}} (\bar{\alpha}_{\mathbf{m}} + i\mathbf{Q}\cdot\bar{\gamma}_{\mathbf{m}} \ldots) e^{i\mathbf{Q}\cdot\mathbf{R}_{\mathbf{m}}} , \tag{7}$$

where

$$\frac{d\sigma}{d\Omega}_{\mathrm{Laue}} = g_0 b_{\mathrm{Fe}}^2 , \tag{8}$$

$$\bar{\alpha}_{\mathbf{m}} = \sum_{s,s'} g_{s,s'}(\mathbf{R}_{\mathbf{m}})/g_0 , \tag{9}$$

$$\bar{\gamma}_{\mathbf{m}} = \sum_{s,s'} \frac{1}{g_0 b_{\mathrm{Fe}}^2} \sum_{i,j} b^i b^j \langle c_s^i(\mathbf{R}) c_{s'}^j(\mathbf{R}')\rangle \mathbf{u}_{\mathbf{m}}{}^{ij} , \tag{10}$$

and

$$\mathbf{u}^{ij}(\mathbf{R}_{\mathbf{m}}) = \frac{\langle c_s^i(\mathbf{R}) c_{s'}^j(\mathbf{R}')[\mathbf{u}(\mathbf{R}_s) - \mathbf{u}(\mathbf{R}'_{s'})]\rangle}{\langle c_s^i(\mathbf{R}) c_{s'}^j(\mathbf{R}')\rangle} \tag{11}$$

is the mean displacement (averaged over both positions and sublattices) between atoms of type i and j at a distance $\mathbf{R}_{\mathbf{m}}$, and $\bar{\alpha}_{\mathbf{m}}$ and $\bar{\gamma}_{\mathbf{m}}$ are Fourier coefficients for short-range order and displacements, normalized with respect to the Laue scattering of both interstitials and vacancies (as done by the authors of Refs. 38 and 11). Thus $\bar{\alpha}_0 \equiv 1$. We have used the same Debye-Waller factors W for Fe and O atoms, $W = B(\frac{Q}{4\pi})^2$, where the temperature factor $B = 3$ Å^2 was chosen for $\mathrm{Fe}_{1-x}\mathrm{O}$, x=0.08, and T=1423 K (see Radler *et al.*[15]).

The usual Cowley-Warren short-range-order parameters for the intrasublattice correlations can be obtained by comparing Eqs. (3) and (9). However, for the intersublattice correlations it appears to be more obvious to interpret those $\bar{\alpha}_{\mathbf{m}}$ by the correlation function $g_{s,s'}(\mathbf{R}-\mathbf{R}')$ as defined by Eq. (1).

Alternatively, and conveniently for our model calculations, we may decompose the actual scattering amplitude into an average and (only) one fluctuating part: $\sum_i b_i c_s^i(\mathbf{R}) = \bar{b}_s + \Delta b_s \Delta c_s(\mathbf{R})$, where $\bar{b}_s = \langle\sum_i b^i c_s^i(\mathbf{R})\rangle_{\mathbf{R}}$ and $\Delta b_s \Delta c_s(\mathbf{R}) = (b_1 - b_2)(c_s^{(1)}(\mathbf{R}) - \bar{c}_s^{(1)})$. If one assumes, for convenience, that $\mathbf{Q}\cdot\mathbf{u}(\mathbf{R}_s) \ll 1$, one has for the diffuse-scattering amplitude

$$\begin{aligned} A(\mathbf{Q})_d &= \sum_{s,\mathbf{R}} \{(\Delta b_s \Delta c_s(\mathbf{R}) + \bar{b}_s)\, e^{-i\mathbf{Q}\cdot\mathbf{u}(\mathbf{R}_s)} - \bar{b}_s\} e^{-i\mathbf{Q}\cdot\mathbf{R}_s} \\ &\simeq \sum_{s,\mathbf{R}} \{\Delta b_s \Delta c_s(\mathbf{R}) - i\mathbf{Q}\cdot\mathbf{u}(\mathbf{R}_s) \\ &\quad \times [\bar{b}_s + \Delta b_s \Delta c_s(\mathbf{R})]\}\, e^{-i\mathbf{Q}\mathbf{R}_s} . \end{aligned} \tag{12}$$

Equation (12) is identical to known expressions, as given for instance by Khachaturyan,[40] apart from labeling various sublattices. It yields intensity expressions [using Eq. (4)] which include the first- and second-order displacement terms and is used for the model calculations in Sec. IV. This formulation is compatible with Eq. (7) or similar expressions used more frequently.[41] For the following Fourier analysis based on Eq. (7) we neglect the second-order displacement terms. Here, in view of the investigated Q range, these are expected to become important only for the Huang scattering close to the Bragg peaks. However, a real-space approach to the Huang scattering would demand an infinite number of parameters for both linear and quadratic displacement terms. On the other hand, the reciprocal space approach in Sec. IV allows for the inclusion of the entire long-range displacement fields and also a consistent treatment of these second-order terms.

B. Fourier analysis

The data for $\mathrm{Fe}_{0.92}\mathrm{O}$ have been analyzed in terms of short-range-order parameters and linear size effect parameters by a linear least squares fitting procedure.[42] We have used the measured data of the (001) and (110) planes.

The level of the Laue scattering is determined by the vacancy and interstitial fractions, or equivalently by the nonstoichiometry x and the vacancy to interstitial ratio ρ. The value $x = 0.079 \pm 0.003$ is obtained from thermogravimetry. ρ has been measured for various compositions and temperatures by Radler *et al.*[15] Extrapolating his data we expect ρ to be 4.5 ± 0.5. The absolute calibration of the scattering data by a vanadium reference enables us also to determine this ratio. Values of $\bar{\alpha}_0$ close to one were found to be consistent with $\rho = 4.0 \pm 0.5$ in agreement with the results of Radler.[15]

The results for the Fourier coefficients of short-range order $\bar{\alpha}_{lmn}$ and of the lattice displacements $\bar{\gamma}_{lmn}$ are listed in the Tables III and IV, respectively.

The diffuse scattering as measured in the (100) and

TABLE III. Fourier coefficients of short-range-order $\bar{\alpha}_{lmn}$ for $\mathrm{Fe}_{0.92}\mathrm{O}$ at T=1423 K. The $\bar{\alpha}_{lmn}$ are distinguished by the types of possible correlations between tetrahedral interstitial sites (int) and substitutional cation sites (sub). Furthermore, the limiting intervals (Min$\bar{\alpha}_{lmn}$, Max$\bar{\alpha}_{lmn}$) due to x and ρ are given. $\bar{\alpha}_{000} = 1.02 \pm 0.09$.

$4\langle lmn\rangle$	$\bar{\alpha}_{lmn}$ int-sub (-0.197, 0.023)	$4\langle lmn\rangle$	$\bar{\alpha}_{lmn}$ sub-sub int-int (-0.095,1)	$4\langle lmn\rangle$	$\bar{\alpha}_{lmn}$ int-int (-0.003, 0.216)
111	-0.174(15)	220	0.215(13)	200	-0.025(18)
311	-0.065(14)	400	0.003(19)	222	0.001(20)
331	-0.031(8)	422	0.016(6)	420	-0.005(16)
333	0.000(3)	440	0.013(7)	600	0.011(26)
511	0.001(5)	620	-0.014(8)	442	0.021(12)
531	0.003(2)	444	-0.030(35)	622	0.006(8)
533	-0.007(5)	642	-0.015(10)	640	0.004(6)
551	0.000(4)	800	-0.002(3)	644	0.006(3)
711	-0.008(8)	660	-0.013(8)	820	0.010(10)
553	0.010(6)	822	0.000(6)	662	0.004(5)
731	-0.002(4)	840	0.008(4)	842	0.000(5)
733	0.000(4)	664	-0.005(2)	1000	-0.003(5)
555	-0.006(3)	844	0.000(2)	666	0.003(5)

(011) planes can be quite well reproduced in nearly all details by the Fourier coefficients $\bar{\alpha}_{\mathbf{m}}$ and $\bar{\gamma}_{\mathbf{m}}$ as shown by the comparison of Figs. 7(a), 7(b), 5(f), and 5(d). The typical error for a data point is 0.2 Laue units, whereas the diffuse data fall into the range of 0.1 up to about 10 Laue units. In principle, it should be possible to improve the description of the measured diffuse intensities by using even more Fourier coefficients to more distant sites and taking further into regard terms which are quadratic in the displacements. This should have only a minor effect on the parameters for the short-range order and displacements as shown in Tables III and IV. However, the present data base is not sufficient for including considerably more Fourier coefficients and therefore, such solutions would become numerically instable.

TABLE IV. Fourier coefficients for linear displacements of $Fe_{0.92}O$ at 1423 K.

$4\langle lmn\rangle$	$\bar{\gamma}_x/Å$	$\bar{\gamma}_y/Å$	$\bar{\gamma}_z/Å$
111	0.009(13)	0.009	0.009
311	-0.009(11)	0.002(10)	0.002
331	-0.031(13)	0.031	-0.007(9)
333	0.035(14)	0.035	0.035
511	0.012(9)	0.000(8)	0.000
531	-0.007(11)	-0.010(10)	-0.010(10)
533	-0.015(8)	-0.015(8)	-0.015
551	-0.009(13)	-0.009	0.000(8)
711	0.012(10)	0.010(10)	0.010
553	0.006(8)	0.006	0.000(8)
731	-0.004(8)	-0.006(8)	0.004(8)
733	0.000(7)	-0.002(7)	-0.002
555	-0.002(7)	-0.002	-0.002

$4\langle lmn\rangle$	$\bar{\gamma}_x/Å$	$\bar{\gamma}_y/Å$	$\bar{\gamma}_z/Å$
220	0.044(11)	0.044	0
400	0.033(11)	0	0
422	0.026(12)	0.017(10)	0.017
440	0.032(9)	0.032	0
620	-0.004(10)	-0.004(10)	0
444	0.024(15)	0.024	0.024
642	0.000(7)	0.000(7)	0.000(7)
800	-0.015(11)	0	0
660	0.009(10)	0.009	0
822	-0.002(9)	0.000(9)	0.000
840	-0.009(9)	-0.004(7)	0
664	0.001(8)	0.001	0.002(6)
844	0.000(6)	0.000(6)	0.000

$4\langle lmn\rangle$	$\bar{\gamma}_x/Å$	$\bar{\gamma}_y/Å$	$\bar{\gamma}_z/Å$
200	-0.057(20)	0	0
222	0.022(20)	0.022	0.022
420	-0.037(17)	-0.026(17)	0
600	0.009(37)	0	0
442	-0.016(12)	-0.016	0.010(10)
622	-0.025(13)	0.004(10)	0.004
640	0.009(12)	-0.002(11)	0
644	0.002(9)	0.000(10)	0.000
820	-0.005(10)	-0.001(9)	0
662	0.000(6)	0.000	0.000(6)
842	0.000(5)	0.000(5)	0.000(5)
1000	0.000(6)	0	0
666	0.006(6)	0.006	0.006

C. Short-range order

Before discussing the short-range-order results it is worthwhile to state the lower and upper bounds for $\bar{\alpha}_{\mathbf{m}}$ for the given defect concentrations for the case of $x = 0.08 \pm 0.001$ and $\rho = 4 \pm 0.5$. For simplicity we consider first the correlations of the type $\alpha_{\{200\}}$ (int-int): The two extremes occur if each interstitial has either no or only interstitials as neighbors at a distance $\mathbf{R}_{\mathbf{m}}$. Since $-c_{\text{int}}^{\text{Fe}}/c_{\text{int}}^{\text{vac}} < \alpha_{\{200\}} < 1$ and $2c_{\text{int}}^{\text{Fe}}c_{\text{int}}^{\text{vac}}\alpha_{\{200\}} = g_0\bar{\alpha}_{\{200\}}$, the upper and lower bounds for $\bar{\alpha}_{\{200\}}$ are given in the present case by $-0.003 \pm 0.0015 < \bar{\alpha}_{\{200\}} < 0.216 \pm 0.03$. Similarly, one obtains the bounds for the correlations of the type $\alpha_{\{220\}}$ (Fe-Fe *and* int-int): $-0.096 \pm 0.005 < \bar{\alpha}_{\{220\}} < 1$ and for the correlations of the type $\alpha_{\{111\}}$ (int-Fe): $-0.196 \pm 0.02 < \bar{\alpha}_{\{111\}} < 0.023 \pm 0.003$.

The short-range-order parameters and also their upper and lower bounds are shown in Fig. 8. The most important result is that α_{111} is close to its lower bound, which means that nearly all interstitials are completely surrounded by Fe vacancies in their nearest neighborhood. Consistently, a large positive value is found for α_{220} indicating a clustering tendency of the vacancies, which is mediated by the interstitials. From these two parameters alone one could deduce a strong support for the 4:1 vacancy-interstitial cluster and maybe also for some of its variants as proposed in the literature. However, the subsequent correlations, in particular of the type 3,

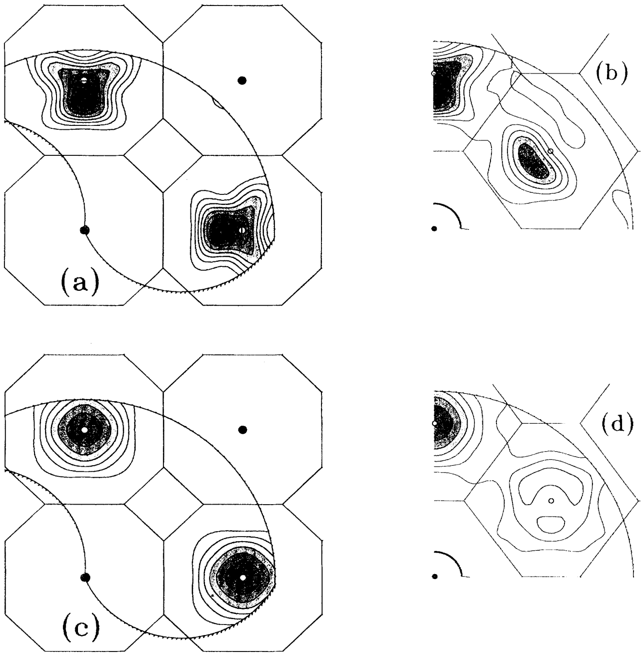

FIG. 7. Contour plots of the recalculated diffuse intensities using the Fourier coefficients $\bar{\alpha}_{lmn}$ and $\bar{\gamma}_{lmn}^{xyz}$, (a) for the (100) plane and (b) for the (110) plane, while (c) and (d) are only the short-range-order contributions due to $\bar{\alpha}$ for the (100) and the (110) planes, respectively. (Contours are also given in steps of 0.1 b/sr.)

interstitials to vacancies, refine this picture as will be discussed in more detail below. As seen in Fig. 8, there is an enhanced probability to find vacancies around an interstitial, not only at nearest-neighbor distances but even up to the third-neighbor shell. One should note that the coefficients $\bar{\alpha}_{\{200\}}$ are rather insensitive to any unlike-neighbor ordering tendency of the interstitials, since the low interstitial concentration renders their lower bound close to zero. The parameter $\bar{\alpha}_{200}$ even falls below this bound. It is, however, within less than two standard deviations still in agreement with a realistic solution. On the contrary, any strong clustering tendency among the interstitials should clearly show up in large positive values, which are not found. Thus the present results suggest that the interstitials are almost randomly dispersed on their sublattice.

Among other diffuse-scattering studies of $Fe_{1-x}O$, the *in situ* x-ray study of Gartstein *et al.*[11] certainly deserves particular attention. Although the nonstoichiometry $x = 0.070 \pm 0.012$ as well as the temperature, $T = 1173$ K, in his work are similar to the present case, the vacancy-interstitial ratio, $\rho = 2.5$, is quite different, and therefore also the appropriate bounds will be different as well. The values for the correlations of types $\bar{\alpha}_{\{220\}}$ and $\bar{\alpha}_{\{111\}}$ agree at least qualitatively with the results here, whereas in this previous work a strong clustering tendency among the interstitials was found in contrast to the present investigation ($\bar{\alpha}_{200} = 0.4 \pm 0.65$, whereas the upper bound is 0.32 as given for a complete interstitial clustering and segregation). Further differences can be revealed by considering the bounds for the other type of short-range-order parameters: For instance, $\bar{\alpha}_{111} = -0.17$ (nearly the same value as found here) is, however, not quite as close to its limit of -0.28, which refers to the case that each interstitial is completely surrounded by only substitutional vacancies. We note that there are indeed significant quantitative and qualitative differences in comparison to the present results. To some extent these differences may result from the different systematic error sources of the two measurements.

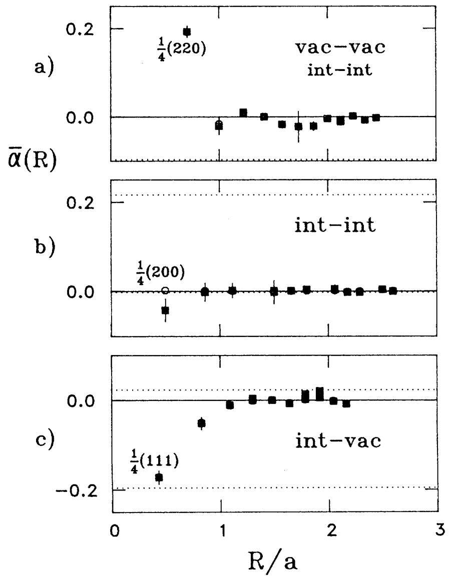

FIG. 8. Short-range-order coefficients $\bar{\alpha}_m$ for $Fe_{0.92}O$ at T=1423 K: results of the Fourier analysis (filled squares) and simulation (open circles, only one can be seen separately and all others coincide). Dotted lines denote lower or upper bounds. (a) Correlations on fcc sublattices; these are dominated by those among vacancies, while a minor contribution comes from those among interstitials at the same distances. For example, vacancy neighbors are favored; (b) the part of correlations on the sc sublattice which is purely among interstitials, showing only random correlations; (c) interstitial to vacancy correlations: e.g., a very strong attraction for close interstitial vacancy neighbors is found.

The short-range-order intensity [Figs. 7(c) and 7(d)] constitutes of even functions [see Eq. (7)] and can of course not reproduce the asymmetries which can be seen in the measured intensity [Figs. 5(f) and 5(d)] and which are due to displacement terms and due to the interference of short-range-order and displacement modulations. This is also true for the position of the diffuse peak at $\mathbf{h} = 1.63(2,0,0)$, which does not shift with the defect content. Nevertheless, it is interesting to trace back parts of the short-range order. While the global maximum around the 200 Bragg peak is mainly due to correlations between nearest interstitials and vacancies described by $\bar{\alpha}_{111}$, the relative minimum inside results from correlations between interstitials to iron as well as from vacancy-iron correlations at further distances. However, in this case further distances mean those beyond the next two shells for the int-vac correlations because of the negative sign of $\bar{\alpha}_{311}$ and $\bar{\alpha}_{331}$. The consequence of the latter two values is that the diffuse maximum is closer confined around the 200. It indicates also that larger aggregates than only randomly distributed 4:1 clusters should exist. The change to a positive sign for $\alpha(\mathbf{R})$ at further distances can be interpreted as the tendency of the charged defects to order and to circumvent themselves with oppositely charged species at further distances, i.e., a self-screening of the defects by short-range ordering (SRO).

For sake of clearness, one should also point out that there is a strong ordering tendency of the defects rather than a clustering tendency among the same defect species. This is consistent for instance with the negative sign of α_{111}, the low intensity around the origin, the large solubility range of the wüstite phase, and the necessity of avoiding large charge fluctuations. There are two mechanisms to reduce the charge fluctuations due to particular defect configurations.

(a) Negatively charged defects (relative to the ideal structure) like Fe vacancies or for instance the $(4{:}1)^{-5}$ cluster maybe less charged because of electron holes or maybe surrounded preferentially by divalent and trivalent Fe ions. This would favor the tendency to small vac-int clusters.

(b) A vacancy sharing of for instance two or more 4:1 clusters reduces the fluctuation of the charge *density* (and also of the scattering density) and may lead to larger defect aggregates.

Both situations are likely to occur. While (a) should be typical for high temperatures and low x, it should be reverse for (b). In view of the balance between large and small defect aggregates in thermal equilibrium, one may note that the vacancy sharing process (b) releases free vacancies to the matrix. Therefore the clustering tendency among the interstitials according to Gartsteins data appears to be plausible rather than obscure.

D. Displacements

In view of the lattice displacements, the actual case of binary solid solutions involving vacancies, though on more than one sublattice, can be analyzed in a straightforward manner, because the vacancies themselves do not contribute directly to the displacement scattering [see Eqs. (7) or (10)]. On the other hand it is still possible to obtain information about the displacements around vacancies. For this purpose, one can use the condition that a mean lattice as well as mean sublattices exist:

$$\sum_{i,j}\langle c_s^i(\mathbf{R})c_{s'}^j(\mathbf{R}')\rangle \mathbf{u_m}^{ij} = 0 \tag{13}$$

for any inter- or intrasublattice vector $\mathbf{R_m} = \mathbf{R}_s - \mathbf{R'}_{s'}$.

If one could expect that the displacements $\mathbf{u}^{ij}(\mathbf{R_m})$ result from a mere size effect, this would permit one to estimate the effective radii of the cation as well as of the vacancy (using for instance $\mathbf{u}^{\mathrm{FeFe}} \approx 2\mathbf{u}^{\mathrm{Fe}}$ and $c_{\mathrm{Fe}}\mathbf{u}^{\mathrm{Fe}} + c_{\mathrm{vac}}\mathbf{u}^{\mathrm{vac}} \approx 0$). However, such an approximation must fail even at a qualitative level if the origins of the displacements are for instance Coulomb forces between the charged ions and vacancies. In this case, and likely it is the present one, $\mathbf{u}^{ij}(\mathbf{R_m})$ should be positive for $i = j$ and negative for $i \neq j$.

For the displacements involving oxygen atoms and using Eq. (13), we have $\mathbf{u}^{\text{O-O}}_{\text{sub-sub}} = 0$, and further $c^{\mathrm{Fe}}_{\mathrm{sub}}\mathbf{u}^{\text{O-Fe}}_{\text{sub-sub}} + (1 - c^{\mathrm{Fe}}_{\mathrm{sub}})\mathbf{u}^{\text{O-vac}}_{\text{sub-sub}} = 0$ and $c^{\mathrm{Fe}}_{\mathrm{int}}\mathbf{u}^{\text{Fe-O}}_{\text{int-sub}} + c^{\mathrm{vac}}_{\mathrm{int}}\mathbf{u}^{\text{vac-O}}_{\text{int-sub}} = 0$, where "sub" denotes "substitutional." (Interstitials may also exert displacements of the fully occupied O sublattice, which was ignored by Hayakawa *et al.*[38] and Gartstein.[11])

We wish to make one observation about the use of parameters such as $\bar{\gamma}_{\mathbf{m}}$ in the present context. In case of x-ray scattering, the parameters $\bar{\gamma}_{\mathbf{m}}$ are not true Fourier coefficients and require an appropriate correction due to the Q dependence of the Fe and O form factors; this is not necessary for neutron scattering because of the Q independence of the scattering lengths. However, a similar correction would be necessary if one wished to account for the different Q dependences of the Debye-Waller factors of the two species.

We can thus deduce the following results from the three types of Fourier coefficients.

Type {220} (Fe-Fe and int-int), for which

$$\begin{aligned}\bar{\gamma}_{\{220\}}g_0 = {}& \langle c^{\mathrm{Fe}}_{\mathrm{sub}}(\mathbf{R})c^{\mathrm{Fe}}_{\mathrm{sub}}(\mathbf{R}')\rangle \mathbf{u}^{\text{Fe-Fe}}_{\text{sub-sub}} \\ &+2\langle c^{\mathrm{Fe}}_{\mathrm{int}}(\mathbf{R})c^{\mathrm{Fe}}_{\mathrm{int}}(\mathbf{R}')\rangle \mathbf{u}^{\text{Fe-Fe}}_{\text{int-int}},\end{aligned} \tag{14}$$

where the second term is negligible since $(c^{\mathrm{Fe}}_{\mathrm{int}})^2 \ll (c^{\mathrm{Fe}}_{\mathrm{sub}})^2$. For instance, from $\bar{\gamma}_{220}$ we thus obtain rather small positive displacements between closest substitutional iron neighbors, $u^{\text{Fe-Fe}}_{\text{sub-sub}} = 0.0093$ Å. The substitutional cations are charged either 2+ or 3+. Their mean charge for the present case is $+2.15|e|$ and the small positive displacements agree with the expected Coulomb repulsion due to the net charges +0.15 of the cations. Similarly one expects $u^{\text{vac-vac}}_{\text{sub-sub}} \geq 0$. Using Eq. (13) yields an estimate for $u^{\text{vac-Fe}}_{\text{sub-sub}} \approx -0.06$ Å.

Type {200} (Fe-O and int-int), for which

$$\begin{aligned}\bar{\gamma}_{\{200\}}g_0 = 2\Bigg(&\frac{b_{\mathrm{O}}}{b_{\mathrm{Fe}}}c^{\mathrm{Fe}}_{\mathrm{sub}}\mathbf{u}^{\text{Fe-O}}_{\text{sub-sub}} \\ &+\langle c^{\mathrm{Fe}}_{\mathrm{int}}(\mathbf{R})c^{\mathrm{Fe}}_{\mathrm{int}}(\mathbf{R}')\rangle \mathbf{u}^{\text{Fe-Fe}}_{\text{int-int}}\Bigg),\end{aligned} \tag{15}$$

where again the second term can be neglected. Although according to Eq. (10) displacements between vacancies and other sites are not visible, we may use Eq. (13) to substitute for $\mathbf{u}^{\text{vac-O}}_{\text{sub-sub}}$. From $\bar{\gamma}_{200}$ it follows that the Fe vacancies repel their nearest oxygen neighbors, $u^{\text{vac-O}}_{200} = (0.10 \pm 0.035)$ Å, which is again to be expected because this defect has a negative net charge with respect to the ideal structure.

Type {111} (int-sub), for which

$$\begin{aligned}\bar{\gamma}_{\{111\}}g_0 = 2\Bigg(&\frac{b_{\mathrm{O}}}{b_{\mathrm{Fe}}}c^{\mathrm{Fe}}_{\mathrm{int}}\mathbf{u}^{\text{Fe-O}}_{\text{int-sub}} \\ &+\langle c^{\mathrm{Fe}}_{\mathrm{int}}(\mathbf{R})c^{\mathrm{Fe}}_{\mathrm{sub}}(\mathbf{R}')\rangle \mathbf{u}^{\text{Fe-Fe}}_{\text{int-sub}}\Bigg).\end{aligned} \tag{16}$$

To a good approximation this provides an estimate of the displacements between interstitials and nearest oxygen neighbors, since in this case there are almost only interstitial-oxygen pairs to be found ($\bar{\alpha}$ is close to the lower bound): $u^{\text{Fe-O}}_{\text{int-sub}} = (0.2 \pm 0.3)$ Å. Therefore it is likely that these displacements are positive, despite having an attractive Coulomb part of their interaction. However, one must also take into regard the repulsive core of the potential, in particular at this closest ion-ion distance. In addition, the average displacement $u^{\text{Fe-O}}_{\text{int-sub}}$ is strongly affected by the other vacancies typically surrounding the interstitial, which repel the oxygens. The positive sign of the interstitial-oxygen displacement thus seems to be reasonable.

Therefore, if we consider a 4:1 cluster for instance, we have to expect its volume to be slightly larger compared to the mean lattice, although there is a general decrease of the lattice parameter per net vacancy. The lattice contraction, however, results from the attraction between cation vacancies and nearest cations. This further agrees with the oxygen parameter $u = 0.2548$ for the neighboring spinel phase Fe_3O_4 being larger than the value 0.25 for an ideal spinel structure.[43] As u increases oxygens around the tetrahedral site displace along a [111] direction. In order to summarize our results on the displacements in $Fe_{0.92}O$, the values we have found agree in magnitude and sign to what can be expected from ion interactions.

E. Modeling of the equilibrium defect structure

The defect correlations were simulated in a computer model of the $Fe_{0.92}O$ structure. All measured SRO parameters were used for this purpose. The model crystal contained 16 simple cubic sublattices each of 9600 sites, four sublattices for the oxygen atoms, four for the iron, and eight for the interstitial sites. Periodic boundary conditions of helical type were applied.[44] The simulation procedure used here (as previously as well[45,46]) is in principle the same as the so-called reverse Monte Carlo method,[47] which has been typically applied to simulate liquid and amorphous structures. The exchange of two atoms is accepted or not with a transition probability given by the sum of the squares of the differences between modeled and measured SRO parameters (instead of an energy difference as in the usual metropolis Monte Carlo method), while in the standard Gehlen-Cohen procedure[48] any exchange is accepted which improves the simulated SRO parameters towards the measured ones. It is found in practice that for the simulation of disordered (or only short-range-ordered) configurations the Gehlen-Cohen procedure also gives representative configurations close to equilibrium if the size of the model crystal is sufficiently large. In the present case corresponding to $Fe_{0.92}O$ our models contained 1024 interstitials and 4096 vacancies which certainly provided a sufficient statistical accuracy in view of the uncertainties in the SRO parameters.

Here we have simulated these different inter- and intrasublattice correlations. This is important for the characterization of the total defect structure. For instance, if one were to leave only the correlations among the interstitials unconstrained in such a simulation, the other types of correlations would induce correlations among the interstitials. (In this case a clustering tendency among the interstitials would be found.) The SRO parameters of the type {220} were assumed to stem from correlations on the Fe sublattice only, since no significant nonrandom values of $\bar{\alpha}$ are found for the pure interstitial correlations, type {200}.

It is noteworthy to state that according to our previous work[49] such a modeling procedure yields the disordered equilibrium structure which is in principle *unique* if the knowledge of the pair correlations is complete.

The resulting modeled structure may be analyzed in various ways. Here, our particular interest is to describe the formation of interstitial-vacancy clusters. For this we need to analyze the connectivity of interstitial and vacancy defects. It is straightforward and simple to obtain the distribution of vacancies having 0–8 nearest interstitial neighbors, or, vice versa, the distribution of interstitials having 0–4 nearest possible vacancy neighbors (Fig. 9). A comparison to the distributions for random configurations (with the same defect content) reveals the strong interaction between interstitials and vacancies. Therefore, most interstitials, namely 64%, are surrounded by the maximum of four vacancies and a further fraction of about 30% interstitials still has three vacancy neighbors.

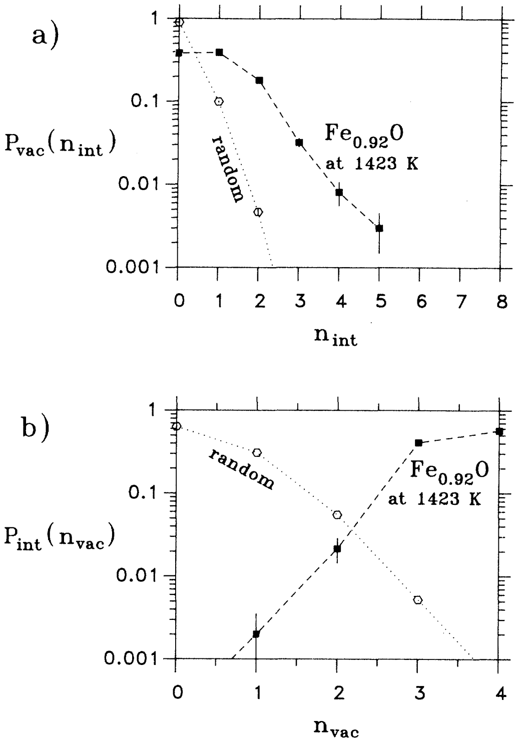

FIG. 9. Results for the modeled defect structure of $Fe_{0.92}O$ at 1423 K (filled squares) in comparison to those for the random configuration. (a) Fraction of vacancies P_{vac} having n_{int} interstitial neighbors. (b) Fraction of interstitials P_{int} having n_{vac} vacancy neighbors. (Lines are only guides for the eye.)

Not as easy to obtain, however, is the cluster size distribution shown in Fig. 10. The algorithm applied here to identify all defect aggregates which are interconnected by vacancy-interstitial "bonds" is similar to the one which has been used in percolation-type problems.[50] One may

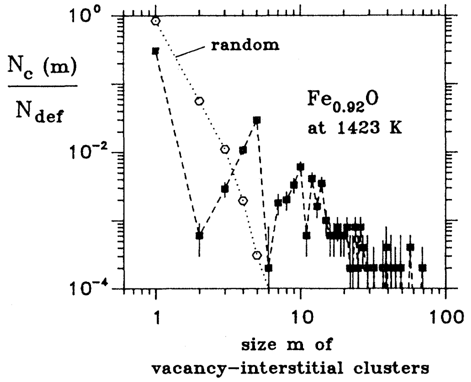

FIG. 10. Size distribution of vacancy-interstitial defect clusters (filled squares) in comparison with the random case (open circles). The size m equals to the total number of vacancies and interstitials in a single isolated cluster, which is interconnected by nearest interstitial to vacancy bonds. $N_c(m)$ equals the number of specific clusters found in the model crystal; N_{def} equals the total number of vacancies and interstitials. (Lines are only guides for the eye.)

further justify the choice of this type of "bond" to define the "clusters" because $\bar{\alpha}_{111}$ is the parameter that is closest to its (lower) bound, indicating that the interaction energies here are particularly important.

There are a few noteworthy results of this type of analysis.

(a) In spite of the strong interstitial-vacancy correlation there is a large fraction of unbound defects. Since the number of unbound (to vacancies) interstitials is vanishingly small (previous Fig. 9) about 40% of the vacancies must be free. This is interesting for the transport properties of this material as will be discussed below.

(b) The particular stability of the 4:1 cluster as predicted theoretically is verified. Note the logarithmic scale and the variation of the distribution density around the cluster size 5. From clusters of size two, a vacancy-interstitial pair, to clusters of size 5, which are nearly all 4:1 clusters, there is an exponential increase in their stability to be found. This is qualitatively in agreement with theoretical predictions.[7] We found that about 3% of the defect clusters are isolated 4:1 defect clusters, or in other words, multiplying with the number of point defects in the cluster, it means that $\approx$ 15% of all point defects, vacancies and interstitials, are bound in isolated 4:1 defect agglomerates.

(c) Larger aggregates exist. They, however, typically incorporate the 4:1 motif as well. Their existence is probably not due to an energetic clustering tendency towards large and compact aggregates; their presence is simply more likely because of the high defect content. Note the discontinuity of the distribution just beyond the size 5, which indicates that it is not energetically favorable to add only one more interstitial to a 4:1 defect cluster.

This analysis does *not*, however, confirm any particular stability of other clusters, which have been proposed in the literature. The likelihood of the 2:1 cluster as proposed by Roth[8] for instance is less than 0.3%. Furthermore, there is no significance found for the so-called Koch-Cohen cluster 13:4, and also the proposed 5:2 cluster by Gartstein, which should consist of two incomplete corner-sharing vacancy tetrahedra aligned along $\langle 110\rangle$ directions, could not be identified as typical at all of the defect structure. These defect clusters have been proposed upon earlier diffuse-scattering experiments. Other even more unlikely defect clusters, like for instance specific 10:4 or even 40:14 clusters[14,13] have been proposed from the interstitial to vacancy ratio as measured from the Bragg intensities (powder Rietveld technique). However, there is no sound basis to deduce the defect arrangements and correlations from only the occupation probabilities of the octahedral (substitutional) and tetrahedral (interstitial) cation sites. Diffuse-scattering experiments, and preferentially elastic diffuse neutron scattering experiments as used in the present case, enable such detailed analyses of defect arrangements.

In particular, this defect cluster distribution offers an explanation of why the cation mobility is so high,[4] $D \approx 10^7$ cm^2/sec at 1000 °C, despite of the strong correlation and binding between interstitials and vacancies. There is a peculiar behavior of the diffusion coefficient since it does not increase with increasing nonstoichiometry, at least for temperatures up to 1000 °C.[4] Because of this, Monty[51] already anticipated that "the diffusion coefficient could be proportional to the concentration of free vacancies in equilibrium with these aggregates of larger cluster following a complex law." In fact and in particular in view of the present results, this view seems to be more realistic than for instance the diffusion mechanisms which have been discussed for the 4:1 clusters.[52]

F. Inverse Monte Carlo results for interaction parameters

A determination of the interaction energies by the inverse Monte Carlo method[53] has been attempted. However, the uncertainties in the experimental measurements, together with strong sensitivities of the interaction energies to some of the short-range-order parameters, have been the reasons why we obtained only rough estimates for the interaction energies.

First, the measurements are not sufficiently sensitive to detect any ordering tendency of the interstitials. This is apparent in view of the lower bounds and error bars for these correlations. Therefore only an upper limit can be estimated for the corresponding interactions. Second, the correlations between vacancies and interstitials are very strong indicating a strong interaction. However, from the error bars for $\bar{\alpha}_{111}$, and in particular those of its lower bound, a coincidence cannot be excluded, which would correspond to an infinite value of the interaction parameter. Results show that the binding energy for a vacancy interstitial pair is at least ≤ -0.2 eV and most likely in the order of -1 eV. The result obtained for a nearest neighbor vacancy pair is about -0.1 eV. However, there is some doubt about the negative sign, since it is contrary to what could be expected from a direct Coulomb interaction. It might indicate, however, that a simple pair wise interaction model is not able to describe the configurational statistics of the defects in such an oxide.

IV. KANZAKI MODEL CALCULATIONS

This section describes how we have calculated the scattering of our defect cluster models, and compares the model results with the experimental ones. Our emphasis is on 4:1 clusters, with a modification made to "decorate" them so as to reduce the long-ranged part of the strain field. We first discuss some general aspects of the calculation of diffuse-scattering intensities from the defect models. Then, we describe the calculation of the displacement fields around defects and their clusters, assuming linear response to the specified forces due to the atoms or defects. Finally, we compare the model results to the experimental data.

A. Calculation of diffuse-scattering intensities

To calculate the diffuse intensities we take the actual displacement at a particular lattice site to result from the displacements fields of all surrounding atoms or defects. (These displacement fields are calculated below in linear response to the defect forces.) In particular, we assume that these fields can be linearly superimposed:

$$\mathbf{u}(\mathbf{R}_s) = \sum_{s',\mathbf{R}'} \Delta c_{s'}(\mathbf{R}')\mathbf{u}_{s'}(\mathbf{R}_s - \mathbf{R}'_{s'}) \ . \tag{17}$$

Inserting Eq. (17) in Eq. (12) gives

$$A(\mathbf{Q}) \simeq \sum_s \Bigg\{ \Delta b_s \Delta c_s(\mathbf{q}) - i\mathbf{Q}\cdot \bar{b}_s \sum_{s'} \Delta c_{s'}(\mathbf{q})\mathbf{u}_{s's}(\mathbf{q}) - i\mathbf{Q}\cdot\Delta b_s \sum_{\mathbf{R}} \sum_{s',\mathbf{R}'} \Delta c_{s'}(\mathbf{R}')\mathbf{u}_{s'}(\mathbf{R}_s - \mathbf{R}'_{s'}) \times \Delta c_s(\mathbf{R}) e^{-i\mathbf{Q}\cdot\mathbf{R}_s} \Bigg\} \ . \tag{18}$$

Here, the first term describes the short-range-order scattering amplitude. The second term describes the part of the scattering amplitude due to displacement fields around an occupational fluctuation $\Delta c_s(\mathbf{R})$, using a mean occupation $\bar{b}_s$ for the surrounding sites. The third term accounts for the fluctuating part $\Delta c_s(\mathbf{R})\Delta b$ of the displaced atoms, which contributes for distances within the range of the short-range order. We have found this term to be of minor importance for our semiquantitative model approach. Therefore, we have finally decided to ignore this third term in the results presented here.

It is useful to note that the Fourier transforms of the displacement fields due to a particular occupation [as used in Eq. (18)]

$$\Delta c_{s'}(\mathbf{q})\mathbf{u}_{s's}(\mathbf{q}) = \sum_{\mathbf{R}_s} \Delta c_{s'}(\mathbf{R}')\mathbf{u}_{s'}(\mathbf{R}_s - \mathbf{R}'_{s'})e^{-i\mathbf{Q}\cdot\mathbf{R}_s} \tag{19}$$

have translational symmetry properties similar to the occupational waves. For simplicity of notation, we will denote (the Fourier transform of) the displacement field of a particular defect by $\mathbf{u}_{\mathrm{def}}(\mathbf{q})$ instead of $\Delta c_{s'}(\mathbf{q})\mathbf{u}_{s's}(\mathbf{q})$.

B. Kanzaki approach to displacement fields

In the present case of nonstoichiometric $Fe_{1-x}O$, we have to consider the effects of cation vacancies and interstitials exerting displacements on the surrounding oxygen and iron ions. However, in a concentrated solid solution not only the "defects," vacancies, and interstitials, but also the host atoms need to be regarded as sources of displacement fields, since they also deviate from the "mean lattice." This will be important for the discussion below, when host atoms are included in the cluster models as well.

As is well known, the displacement fields are of infinite range because of the elastic properties of the crystal. The basic idea of Kanzaki-force models is to reproduce the long-range displacement fields by using forces on only a few shells of neighbors, whose magnitudes are fixed by known parameters and a few physically motivated approximations. The displacement field in response to these forces is calculated using the linear response of the atomic positions. This approach has been applied mainly to dilute alloys,[54–61] but also to concentrated alloys.[62,63] Furthermore, in most applications either only the long-wavelength limit and/or only main symmetry directions are discussed, where one can simply refer to the measured phonon frequencies. Here the overall description of the diffuse scattering requires the calculation of the full dynamical matrix, which was performed using a program of Eckhold.[64]

The major assumption is the following:

$$\mathbf{u}_{\mathrm{def}}(\mathbf{q}) = \mathbf{\Phi}(\mathbf{q})^{-1}\mathbf{F}_{\mathrm{def}}(\mathbf{q}) \ . \tag{20}$$

Here we write $\mathbf{u}_{\mathrm{def}}(\mathbf{q})$ as a six-component vector containing the (vector) displacement fields of the Fe and O atoms due to the defect, which may be an interstitial, a vacancy, an empty interstitial site, or a substitutional Fe atom, so that $\mathbf{u}_{\mathrm{def}}(\mathbf{q}) = \{\mathbf{u}^{\mathrm{Fe}}_{\mathrm{def}}(\mathbf{q}_s), \mathbf{u}^{\mathrm{O}}_{\mathrm{def}}(\mathbf{q}_{s'})\}$. Similarly, $\mathbf{F}_{\mathrm{def}}(\mathbf{q})$ is defined as a six-component vector of the Fourier transforms of the forces exerted by the defects, so that

$$\mathbf{F}_{\mathrm{def}}(\mathbf{q}) = \sum_s \Delta c_s(\mathbf{q})\mathbf{F}_s(\mathbf{q}) \ . \tag{21}$$

$\mathbf{F}_s(\mathbf{q})$ is the Fourier transform of the force associated with a single defect on sublattice s, relative to the perfect lattice. Since Δc has opposite sign for vacancies and host atoms, the forces around vacancy and host atoms are of opposite sign. We note further that within a single-defect approximation, where the ideal lattice is the reference medium, it is sufficient to consider only the forces exerted by the defect, because those of the host atoms vanish.

The force-constant matrix $\mathbf{\Phi}$ is related to the usual dynamical matrix by

$$\mathbf{\Phi}(\mathbf{q}) = \mathbf{M}^{1/2}\mathbf{D}(\mathbf{q})\mathbf{M}^{1/2}. \tag{22}$$

It is composed of four 3×3 blocks corresponding to Fe-Fe, Fe-O, O-Fe, and O-O interactions, where, for example,

$$\mathbf{\Phi}^{\mathrm{Fe,O}}(\mathbf{q}) = \sum_{\mathbf{R}'} \mathbf{V}^{\mathrm{Fe,O}}(\mathbf{R},\mathbf{R}') \exp\{-i\mathbf{Q}\cdot(\mathbf{R}-\mathbf{R}')\}. \tag{23}$$

Here $\mathbf{V}^{\mathrm{Fe,O}}(\mathbf{R},\mathbf{R}')$ is the force-constant matrix corresponding to relative motions of Fe and O atoms at $\mathbf{R}$ and $\mathbf{R}'$; $\mathbf{R}$ is any Fe site, and $\mathbf{R}'$ are the O sites. Similar expressions are obtained for the other three blocks of $\mathbf{\Phi}$. One should note that this force-constant matrix $\mathbf{\Phi}$ contains no information about the lattice couplings between the substitutional and interstitial sites. Therefore we cannot include the scattering contribution due to displaced interstitials in this approach. However, because of the comparatively small fraction of occupied interstitial sites this contribution is of minor importance and will be neglected here.

C. Force constants

To obtain the force-constant matrix $\mathbf{\Phi}(\mathbf{q})$ for FeO, we use the "shell model" of the interactions. The underly-

TABLE V. Shell-model parameters used to calculate the force constant matrix $\mathbf{\Phi}$. The data are close to the values of model IV of Kugel *et al.* (Ref. 65) and describe their experimental data of the phonon dispersion of FeO at room temperature.

	Atomic masses	Ion charges	Shell charges	Polarizabilities
Fe	55.85	$1.587e$	$2.46e$	1.0790 Å^3
O	16.00	$-1.587e$	$-2.81e$	1.3283 Å^3
Shell-shell force constant				
	Longitudinal		131.14	Nm^{-1}
	Transverse		-21.69	Nm^{-1}

ing picture is that of charged ions, each of which has an electronic shell that can be displaced relative to the ion core. The ionic polarizability comes from such displacements. The types of interactions that are included, and whose values are specified in Table V, are the following: (1) direct Coulomb interactions between nuclei and shells on one atom, with those on other atoms; (2) intra-atomic core-shell interactions, which give a restoring force that is linear in the relative displacement of core and shell; and (3) repulsive overlap interactions between nearest neighbor shells, specified by longitudinal and transverse force constants.

In view of the charged defects in the nonstoichiometric $Fe_{1-x}O$ such as electron holes, vacancies in probably different charged states and interstitials, in principle one should better use a screened rather than an unscreened Coulomb interaction. However, one should regard the above model just as an approximate and convenient description of the dynamical matrix, which is consistent with the phonon data found in the literature.[65]

D. Choice of Kanzaki forces

We disregard the direct contribution from long-ranged Coulomb interactions to the Huang scattering, which was discussed by Gillan.[66] This would be important for very dilute systems, but in the present case of a highly concentrated defect system, it is likely that the Coulomb interactions will be screened, and this contribution will tend to vanish. We use short-ranged Kanzaki forces, which cannot yield a quantitative fit to the data, but do explain the major features of the observed scattering intensities.

We use three considerations in determining the force parameters.

(1) The separation between an Fe interstitial atom and the neighboring O atoms, which we obtain in the absence of relaxations, is very close to the measured value of this separation in the spinel phase. Thus we ignore direct forces from the interstitials. This is plausible in view of their charge of +3, and therefore being smaller than the NaCl sublattice Fe atoms.

(2) The observed vacancy relaxation volume ΔV provides a constraint on the atomic forces around a vacancy. To explain the implementation of this constraint, we first ignore the effects of interstitials. We have, in linear order,[57] that

$$P = \sum_{\mathbf{R}} \mathbf{R} \cdot \mathbf{F}_{\text{vac}}(\mathbf{R}) = 3pV = 3B\Delta V = 22.1 \text{ eV}, \quad (24)$$

where we have used the measured bulk modulus B=1.94 Mbar (Ref. 65) and the known lattice parameter change[15] yielding the relaxation volume per net vacancy ΔV = 6.2 Å^3. However, because the elastic constants of our model do not precisely match the experimental ones, we modify P to improve the value of the Huang scattering intensity at small q. This intensity is proportional to $(P/C_{11})^2$, where C_{11} is the longitudinal elastic constant. Therefore, if we assumed only vacancies, the correct Huang scattering would be obtained by taking $P^{\text{model}} = P(C_{11}^{\text{model}}/C_{11}) = P(2.85/3.0 \text{ Mbar})=$ $0.95P = 21.0$ eV, where the experimental C_{11} value is taken from.[65] (Note that we ignore temperature-induced changes in the elastic constants. If we assume that the fractional changes in B and C_{11} are equal, then they will not affect the the ratio P/C_{11} entering the Huang scattering, since P is proportional to B.)

The effects of interstitials complicate the situation, because the measured relaxation volume per vacancy is given in terms of the *net* vacancy count, where the interstitial count is subtracted off. Since we set interstitial forces equal to zero, this effect can be taken into account by, for each cluster, reducing P by a factor $N_{\text{vac}}^{\text{net}}/N_{\text{vac}}^{\text{tot}}$. So, for a model based on 4:1 clusters, we use $P = 21.0 \text{ eV} \times [(4-1)/4] = 15.8$ eV.

(3) The rough magnitudes of the forces are estimated on the basis of Coulomb interactions to be on the order of 1 eV/Å, which lead to nearest neighbor displacements in the order of 0.1 Å. Furthermore, Coulomb interactions suggest that vacancy forces on oxygen atoms should be repulsive, and those on iron atoms attractive.

With these considerations in mind, we have chosen the following set of nearest-neighbor force parameters:

$$\begin{aligned} F_{\text{vac}}^{\text{O}} &= -1.6 \text{ eV/Å} \times (-\bar{c}_{\text{sub}}) \text{ repulsive}, \\ F_{\text{vac}}^{\text{Fe}} &= 1.0 \text{ eV/Å} \times (-\bar{c}_{\text{sub}}) \text{ attractive}, \\ F_{\text{int}}^{\text{O}} &= F_{\text{int}}^{\text{Fe}} = 0 . \end{aligned} \quad (25)$$

Note that with respect to the mean lattice of a solid solution, not only vacancies or interstitials but also occupied Fe sites have to be considered as defects. In the case of occupied Fe sites, the forces $\mathbf{F}_{\text{Fe}}$ are obtained by multiplying the ideal-lattice forces by the occupational fluctuation $\Delta c_{\text{Fe}} = 1-\bar{c}_{\text{sub}}$ [instead of by $(-\bar{c}_{\text{sub}})$]. These force parameters will be applied for all defect models treated, using the appropriate superposition for each model. A schematic picture, cf. Fig. 11, shows the Kanzaki forces which a cation vacancy exerts upon the neighboring oxygen and iron ions.

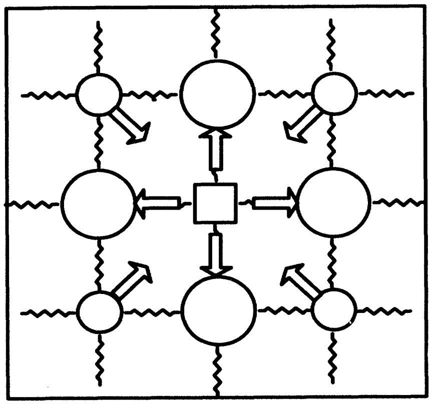

FIG. 11. Schematic representation of the Kanzaki-force model of a cation vacancy defect. Nearest oxygen ions are repelled and the next nearest iron ions are attracted. The displacement field around the defect, which is calculated in linear response to these forces, is of long range due to the lattice couplings, described by the force-constant matrix $\mathbf{\Phi}$ consistent with independent phonon data.

E. Defect cluster models

The defect clusters that we shall consider are simple vacancies and 4:1 clusters as defined above. As discussed in the Introduction, the 4:1 cluster is supported by a substantial body of experimental evidence and theoretical evidence, although in many cases only as a basic element of more complex defect arrangements. We note that the approximation of using defect clusters is only a crude approximation to the real correlations in a system. It is appealing because it provides a simple visualization of coherently scattering-defect arrangements. However, the assumed cutoff of correlations is not very realistic. In addition, we expect some of the clusters to split up partially at higher temperatures. One could, in principle, use the measured correlation functions, together with the formalism developed above, to calculate the diffuse scattering. However, we have found this approach to be impractical and have not implemented it.

We consider two variants of the 4:1 cluster. In the first, the "isolated 4:1 cluster" only the correlations inside the cluster are retained, and the scattering is measured relative to the ideal lattice. This model gives a concentration dependence of the diffuse-scattering intensity that is rigorously linear. We also consider a "decorated cluster" model in which a 4:1 cluster is definitely surrounded by two shells of iron instead of possibly having vacancy neighbors in these sites. (Note that this simplifying choice is, however, not quantitatively consistent with the observed short-range-order parameters. A more realistic but also then much more complicated model should be able for instance to reproduce also precisely the wave vectors of the observed diffuse peaks.) We thus take into account Fe occupations in the second and third cation shells $1/4\{3,1,1\}$ and $1/4\{3,3,1\}$ around the central interstitial. The scattering is measured relative to the mean lattice. This model is motivated by the above results for 1150 °C, in which the overall intensities have a substantial nonlinear component in the concentration dependence. In particular, the Huang scattering does not increase with the defect concentration but seems to disappear instead. We attribute the (relatively) reduced Huang scattering to mutual screening of the long-ranged parts of the strain and electrostatic fields of the defects. The decoration of the 4:1 cluster is a simple way of modeling this screening.

The decorated cluster model is treated by the above formalism, where each of the surrounding irons has a force proportional to $1 - c_{\text{sub}}$, with a sign opposite to the vacancy force. Note that this gives a nonlinear concentration dependence of the scattering, both through the concentration dependence of the vacancy forces and that of the Fe forces. However, any further correlations in the spatial distribution of these clusters are neglected in the model calculations.

F. Results and comparison with experiment

Before we present our model results and compare them with the experimental data, we give a short qualitative discussion of the measured diffuse scattering to point out the characteristic features, which can be related to specific defect arrangements and associated displacements. For simplicity, we assume the ideal lattice to be the reference, i.e., $\bar{c}_s = 1$ and 0 for the substitutional and for the interstitial lattices, respectively. One then finds that at the scattering vector $\mathbf{Q} = 0$ the amplitude $A(0)$ is proportional to the *difference* of the numbers of vacancies and interstitials of coherently scattering objects like clusters, while for instance at $\mathbf{Q} = \frac{2\pi}{a}(2,0,0)$ for the present structure (NaCl) it is the *sum* of vacancies and interstitials which matters. While the symmetry properties of the fcc cation sublattice, relevant for the vacancy correlations, are indicated in Fig. 9 and in all contour plots shown by the Brillouin zones of the bcc reciprocal sublattice with zone centers at $\mathbf{G_{hkl}}$ with h,k,l all even or odd, the correlations between interstitials and cation vacancies (on a real-space bcc sublattice) refer to a larger fcc unit cell in reciprocal space with all h,k,l even and $\text{Mod}(h+k+l,4) = 0$ (h,k,l are used throughout with respect to the FeO unit cell).

These considerations enable us to draw a few conclusions from the observed diffuse intensities.

(1) Large densely packed clusters of vacancies and interstitials, having a vacancy to interstitial ratio significantly larger than one, are not present in large numbers. Such clusters would produce a significant scattering around $\mathbf{Q} = 0$ which is not observed.

(2) Correlated tetrahedral interstitials and substitutional vacancies exist, since the diffuse scattering is stronger around $\mathbf{h} = (2,0,0)$ than around $\mathbf{h} = (0,0,0)$ or $\mathbf{h} = (2,2,0)$.

(3) Displacement effects are very important. The lack of symmetry of the diffuse scattering, for instance across the mirror plane perpendicular to $\mathbf{h} = (2,0,0)$, cannot

be described by any short-range ordering, but must stem from the scattering due to the displacements in the system, and in particular due to the displacements around the cation vacancies. Displacements around the interstitials create the observed more complex asymmetry of the scattering across the Brillouin zones for the correlations between interstitials and the ions on the regular fcc sublattices. These lines of high symmetry are nodes for the odd functions of the linear size effect scattering.

We now turn to the calculated diffuse-scattering intensities, and comparison with the experiment. Since the defect concentrations are very large in $Fe_{1-x}O$, we expect the use of the mean lattice rather than the ideal lattice to have a substantial impact. We first consider results from a model containing only vacancies (no interstitials), to illustrate further the necessity of interstitials in explaining the observed scattering. Figures 12(a) and 12(b) show results for the vacancy model and for the 4:1 cluster, respectively. The intensities are calculated for $x = 0.08$. However, they scale linearly with x within the single-defect approximation (ideal lattice reference). It can be seen that the calculated diffuse intensities are rather weak for the vacancy-only model and that also the pattern is not consistent with the shape of the observed intensities. On the other hand, since the scattering is comparatively weak this result does not exclude the existance of free vacancies as found in the analysis of Sec. III E.

Figure 12(b) shows model results for the 4:1 cluster. By comparison with Fig. 5(f), we see that the agreement is much better than for the vacancy case. The distribution of overall intensities between the (0, 0, 0), (2, 0, 0), and (2, 2, 0) is consistent with the observations. In addition, the shape of the scattering around the (2, 0, 0) and (2, 2, 0) peaks is well obtained, with characteristic features emerging diagonally out from the (2, 0, 0) peak. The main feature that is not obtained by these results is the diffuse peak at the low Q side of the (2, 0, 0) Bragg peak that is seen in Figs. 5(d)–5(h); rather, in the model calculations, the intensity diverges smoothly near the Bragg peak, as is expected from Huang scattering.

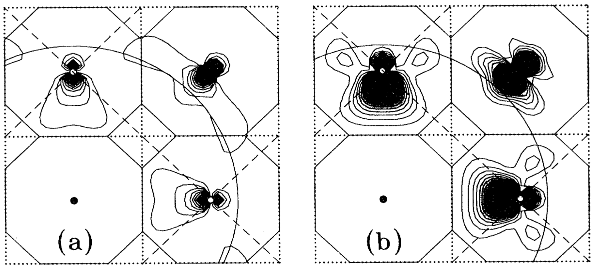

FIG. 12. Diffuse-scattering intensities for $Fe_{1-x}O$ as calculated by a Kanzaki model approach to the long-range displacement fields (a) of only random cation vacancies for the largest nonstoichiometry $x = 0.13$, and (b) of the 4:1 defect cluster at $x = 0.08$, both within the single-defect approximation. Contours in steps of 0.1 b/sr. Brillouin zones are also shown for the fcc sublattice, and (dashed line) for the correlations between interstitials and ions on the fcc sublattices.

As mentioned above, the reduced Huang scattering in the experimental data is likely due to short-range-order effects screening the strain and electrostatic fields of the defects. For an appropriate treatment it requires to use a Kanzaki model valid for solid solutions and to renounce on the single-defect approximation. In order to mimic qualitatively the short-range-order effects, we thus now turn to the "decorated" 4:1 cluster model discussed above. Results for all four measured concentrations are shown in Figs. 13(a)–13(d). Comparison of the $x = 0.08$ results with those of the previous model approach shows that the Huang scattering effects are indeed substantially reduced. A strong nonlinearity in the concentration dependence is also observed, with the shape of the scattering changing substantially as one goes from $x = 0.054$ to $x = 0.13$. Comparison [of Figs. 13(a)–13(d) with the corresponding Figs. 5(e)–5(h)] shows that the agreement with experiment is markedly improved. The results for the (110) plane, indicated in Fig. 13(e), also show good agreement with the experimental results of Fig. 5(d).

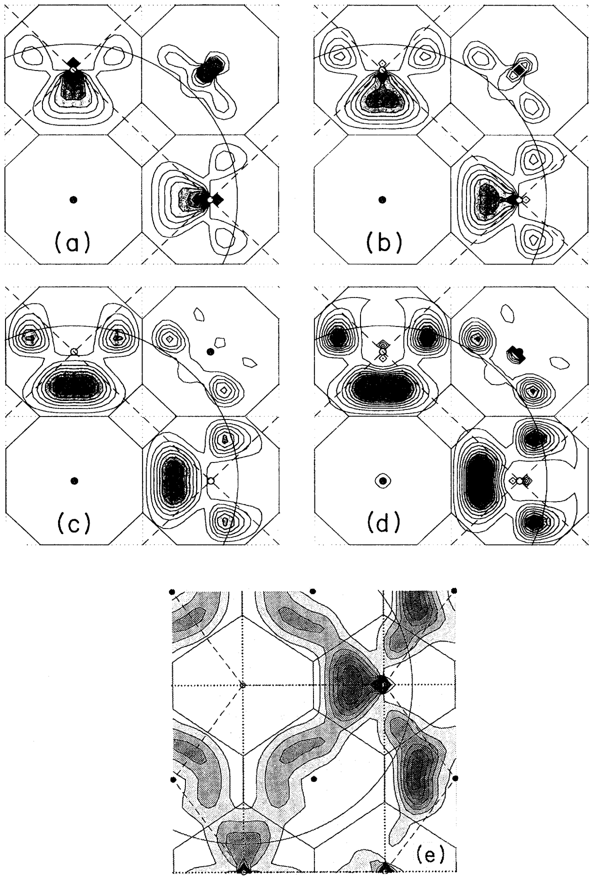

FIG. 13. Diffuse scattering intensities for $Fe_{1-x}O$ as calculated by a Kanzaki model approach to the long-range displacement fields of the 4:1 defect cluster, whose next two cation shells are fully occupied, while the mean lattice was taken as the reference. Results for the (100) plane at (a) $x = 0.054$, (b) $x = 0.08$, (c) $x = 0.104$, (d) $x = 0.13$, and (e) for the (110) plane at $x = 0.08$. (Contours and Brillouin zones as in Fig. 12.)

V. SUMMARY AND CONCLUSION

In summary, we have measured *in situ* the diffuse neutron scattering from $Fe_{1-x}O$, over a range of defect concentrations and temperatures. By Fourier analysis of one particular data set, for $x = 0.08$ and $T = 1423$ K, short-range order and displacement parameters were obtained. A simulation of the equilibrium defect structure was performed using all of the measured short-range-order parameters. A proper statistical analysis of the modeled structure yielded a detailed size distribution of the vacancy-interstitial clusters. We have demonstrated a pronounced tendency toward the formation of 4:1-type clusters, although a substantial concentration of free vacancies is present as well. This particular noteworthy result shows that at thermal equilibrium the predicted high stability of defect clusters based on the 4:1 motif is not controversial to the existence of a large fraction of free vacancies, being necessary to explain for the high cation mobility. In fact, about 40% of the defects are bound in even larger clusters than the 4:1 cluster. However, as can be seen also from the rather low scattering intensities at small angles, such larger aggregates should not have a compact shape and their appearance should be mainly a consequence of the high defect concentration. In the present study, we have not attempted to analyze the growth mechanism of such clusters. Such questions may be a good subject for similar studies in particular at even higher nonstoichiometries, where we have collected up to now only data in the (100)-scattering plane, which are insufficient for this purpose.

In view of a possible consistent modeling of the phase stabilities of wüstite and magnetite, our results by the inverse Monte Carlo simulation for the interatomic interactions are certainly not of sufficient quantitative precision. However, the large solubility of defects in wüstite and the high stability of the 4:1 cluster, a structural motif not only of the defect structure of wüstite but also of the ideal magnetite structure, should be consistent with an interaction model which is dominated by strong short-range interactions of ordering type.

The observed asymmetry of the diffuse-scattering intensities around the Bragg peaks was shown to arise mainly from the displacement fields around the cation vacancies, which due to the missing charges at those sites repel the nearest oxygen ions and attract the next neighbored cations. In analogy to the description of phonon modes, one could say these static displacements have an optical character with inversion symmetry. Hence, the displacements around the cation vacancies turned out to be at least qualitatively as expected from Coulomb interactions. In contrast to this, the displacements of the oxygens around the interstitials seem to be more determined by hard core repulsion of the ions.

In order to include the entire long-range displacement fields of the defects and to understand in particular the surprisingly low Huang scattering, we have performed Kanzaki-force calculations of the diffuse scattering based and motivated on the above-mentioned results of the short-range order. We considered both "isolated" 4:1 clusters in a usual Kanzaki model as typically applied to the dilute defect case, as well as "decorated" 4:1 clusters, surrounding the 4:1 cluster with two shells of regular cations, where we applied a more general formalism being valid also for the concentrated defect case. The isolated-cluster results obtain most of the major features of the experimental results. However, using a comparatively simple model with a least number of parameters the decorated-cluster results well describe the observed changes in the scattering pattern with increasing nonstoichiometries x. These are the apparent decrease of the Huang scattering with increasing x and the development of diffuse peaks at $\mathbf{h} = 0.82(2,0,0)$ and $\mathbf{h} = 0.82(1,1,1)$, which lack of symmetry properties valid for short-range order only. The decrease of the Huang scattering with x can be understood to result from the mutual screening of the defects by short-range ordering, which also means a screening of their charges and their strain fields. Finally, the similarity of the observed diffuse scattering for the investigated part of the wüstite phase field and the consistent results of the model calculations based on an invariant model verify the homogeneity of this phase, which has sometimes been suspected.[67–70]

ACKNOWLEDGMENTS

This work was supported by the BMFT under the Contract No. 03-MA3HAN-0 (A.H.), by the United States Department of Energy under Grant No. DE-FG02-84ER45130 (A.C.), and by the Alexander von Humboldt Stiftung which enabled A.C. to visit Jülich during the time of this collaborative work.

---

* Present address: Institut für Physikalische Chemie , Elektrochemie, TH Darmstadt, Petersenstr. 20, D-64287 Darmstadt, Germany.

[1] A. Muan and E.F. Osborn, *Phase Equilibria Among Oxides in Steelmaking* (Addison-Wesley Publishing Company, Inc., Reading, MA, 1965).

[2] L.S. Darken and R.W. Gurry, J. Am. Chem. Soc. **67**, 1398 (1945).

[3] S. Yamaguchi and M. Someno, Trans. Jpn. Inst. Metals **23**, 259 (1982).

[4] W.K. Chen and N. Peterson, J. Phys. Chem. Solids **36**, 1097 (1975).

[5] C.R.A. Catlow and A.M. Stoneham, J. Am. Ceram. Soc. **64**, 234 (1981).

[6] R.W. Grimes, A.B. Anderson, and A.H. Heuer, J. Am. Ceram. Soc. **69**, 619 (1986).

[7] M.R. Press and D.E. Ellis, Phys. Rev. B **35**, 9 (1987); **35**, 4438 (1987).

[8] W.L. Roth, Acta Crystallogr. **13**, 140 (1960).

[9] F. Koch and J.B. Cohen, Acta Crystallogr. B **25**, 275 (1969).

[10] M. Hayakawa, M. Morinaga, and J.B. Cohen, in *Defects and Transport in Oxides*, edited by M.S. Seltzer and R.I. Faffee (Plenum Press, New York, 1973), p. 177.

[11] E. Gartstein, T.O. Mason, and J.B. Cohen, J. Phys. Chem. Solids **47**, 759 (1986).

[12] A. K. Cheetham, B.E.F. Fender, and R.I. Taylor, J. Phys. C **4**, 2160 (1971).

[13] J. R. Gavarri, C. Carel, and D. Weigel, J. Solid State Chem. **29**, 81 (1979).

[14] C. Carel and J.-R. Gavarri, J. Phys. Chem. Solids **51**, 1131 (1990).

[15] M. Radler, J.B. Cohen, and J. Faber, Jr., J. Phys. Chem. Solids **51**, 217 (1990).

[16] C. Lebreton and L.W. Hobbs, Radiat. Eff. **74**, 227 (1983).

[17] B. Anderson and J. O. Sletnes, Acta Crystallogr. A **33**, 268 (1977).

[18] M. Labidi and C. Monty, Phase Trans. **31**, 99 (1991).

[19] N.N. Greenwood and A.T. Howe, J. Chem. Soc. Dalton Trans. **1**, 122 (1972).

[20] Z. Inglot, D. Wiarda, K.P. Lieb, T. Wenzel, and M. Uhrmacher, J. Phys. Condens. Matter **3**, 4569 (1991).

[21] J. Nowotny and M. Rekas, J. Am. Ceram. Soc. **72**, 1221 (1989).

[22] I. Bransky and A.Z. Hed, J. Am. Ceram. Soc. **57**, 231 (1968).

[23] A. Madouri and C. Monty, Adv. Ceram. **23**, 86 (1987).

[24] F. Adam, B. Dupre, D. Gleitzer, and J. Nowotny, J. Phys. Chem. Solids **51**, 1123 (1990).

[25] M. Seltzer and A.Z. Hed, J. Electrochem. Soc. **117**, 815 (1970).

[26] H. K. Bowen, D. Adler, and B. H. Auker, J. Solid State Chem. **12**, 355 (1975).

[27] E. Jolles and C. Monty, Philos. Mag. A **64**, 765 (1991).

[28] E. Gartstein, J.B. Cohen, and T.O. Mason, J. Phys. Chem. Solids **47**, 775 (1986).

[29] M. Rekas and S. Mrowec, Solid State Ionics **22**, 185 (1987).

[30] W. Schweika, A. Hoser, and M. Martin, Ber. Bunsenges. Phys. Chem. **96**, 1541 (1992).

[31] D. Schuster, Thesis, KFA Forschungszentrum Report No. JÜL-2278, 1989.

[32] J.F. Elliott and M. Gleiser, *Thermochemistry of Steelmaking* (Addison-Wesley Publishing Co., Inc., Reading, MA, 1960).

[33] D. Schuster, R. Dieckmann, and W. Schweika, Ber. Bunsenges. Phys. Chem. **93**, 1347 (1989).

[34] The time-of-flight data analysis was efficiently supported by the internal TOFSYS software supplied by M. Monkenbusch, IFF.

[35] A. Yamamoto, Acta Crystallogr. B **38**, 1451 (1982).

[36] M.J. Radler, J.B. Cohen, G.P. Sykora, T. Mason, D.E. Ellis, and J.F. Faber, J. Phys. Chem. Solids **53**, 141 (1992).

[37] V. F. Sears, Neutron News **3**, 26 (1992).

[38] M. Hayakawa and J.B. Cohen, Acta Crystallogr. A **31**, 635 (1975).

[39] B.E. Warren and B.L. Averbach, *Modern Research Techniques in Physical Metallurgy* (ASM, Cleveland, 1953), pp. 95–130; B.E. Warren, *X-Ray Diffraction* (Dover, New York, 1990).

[40] A.G. Khachaturyan, *Theory of Structural Investigations in Solids* (John Wiley & Sons, New York, 1983).

[41] L.H. Schwartz and J.B. Cohen, *Diffraction from Materials* (Springer, Berlin, 1987).

[42] C.L. Lawson and R.J. Hanson, *Solving Linear-Least Squares Problem* (Englewood Cliffs, New Jersey, 1974); R.O. Williams, Metall. Trans. **5**, 1843 (1974).

[43] H.St.C. O'Neill and A. Nauvrotsky, Am. Mineral. **68**, 181 (1983).

[44] W. Schweika, in *Structural and Phase Stability of Alloys*, edited by J.L. Moran-Lopez, F. Mejia-Lira, and J.M. Sanchez (Plenum Press, New York, 1992), pp. 53–64.

[45] W. Schweika and H.-G. Haubold, Phys. Rev. B **37**, 16 (1988); **37**, 9420 (1988).

[46] W. Schweika, in *Alloy Phase Stability*, Vol. 163 of *NATO Advanced Study Institute, Series E: Applied Science*, edited by G.M. Stocks and A. Gonis (Kluwer, Dordrecht, 1989), p. 137.

[47] R.L. McGreevy and L. Pusztai, Mol. Simmulation **1**, 359 (1988).

[48] P.C. Gehlen and J.B. Cohen, Phys. Rev. **139**, A844 (1965).

[49] W. Schweika and A.E. Carlsson, Phys. Rev. B **40**, 4990 (1989).

[50] J. Hoshen and R. Kopelman, Phys. Rev. B **14**, 3428 (1976).

[51] C. Monty, in *Diffusion in Materials*, Vol. 179 of *NATO Advanced Study Institute, Series E: Applied Science*, edited by A.L. Lasker, J.L. Bocquet, and C. Monty (Kluwer Academic Publ., Dordrecht).

[52] A.M. Stoneham, Phys. Today **33**, 34 (1980).

[53] V. Gerold and J. Kern, Acta Metall. **35**, 393 (1987).

[54] T.J. Matsubara, J. Phys. Soc. Jpn. **7**, 270 (1952).

[55] H. Kanzaki, J. Phys. Chem. Solids **2**, 24 (1957); **2**, 107 (1957).

[56] H. Trinkaus, Phys. Status Solidi B **51**, 307 (1972).

[57] P. Dederichs, J. Phys. F **3**, 471 (1973).

[58] P. Ehrhart, H.G. Haubold, and W. Schilling, Adv. Solid State Phys. **14**, 87 (1974).

[59] G.S. Bauer, E. Seitz, and W. Just, J. Appl. Crystallogr. **8**, 162 (1975).

[60] M.S. Blanter and A.G. Khachaturyan, Metall. Trans. **9A**, 753 (1978).

[61] M.S. Blanter, Phys. Status Solidi B **181**, 377 (1994).

[62] H.E. Cook, J. Phys. Chem. Solids **30**, 1097 (1969).

[63] W. Schweika, in *Statics and Dynamics of Alloy Phase Transformations*, Vol. 319 of *NATO Advanced Study Institute, Series B: Physics*, edited by P.E.A. Turchi and A. Gonis (Plenum Press, New York, 1994), p. 103.

[64] G. Eckhold, JÜL-2639 report of the KFA Forschungszentrum Jülich, 1992.

[65] G. Kugel, C. Carabatos, B. Hennion, B. Prevot, A. Revcolevschi, and D. Tochetti, Phys. Rev. B **16**, 378 (1977).

[66] M.J. Gillan, Philos. Mag. A **53**, 415 (1986).

[67] P. Vallet and P. Raccah, Compt. Rend. **258**, 3679 (1964).

[68] P. Vallet and P. Raccah, Mem. Sci. Rev. Met. **62**, 1 (1965).

[69] B.E.F. Fender and F. D. Riley, J. Phys. Chem. Solids **30**, 793 (1969).

[70] E. Takayama and N. Kimizuka, J. Electrochem. Soc. **127**, 970 (1980).

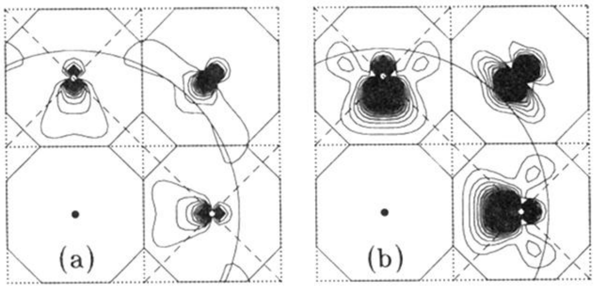

FIG. 12. Diffuse-scattering intensities for $Fe_{1-x}O$ as calculated by a Kanzaki model approach to the long-range displacement fields (a) of only random cation vacancies for the largest nonstoichiometry $x = 0.13$, and (b) of the 4:1 defect cluster at $x = 0.08$, both within the single-defect approximation. Contours in steps of 0.1 b/sr. Brillouin zones are also shown for the fcc sublattice, and (dashed line) for the correlations between interstitials and ions on the fcc sublattices.

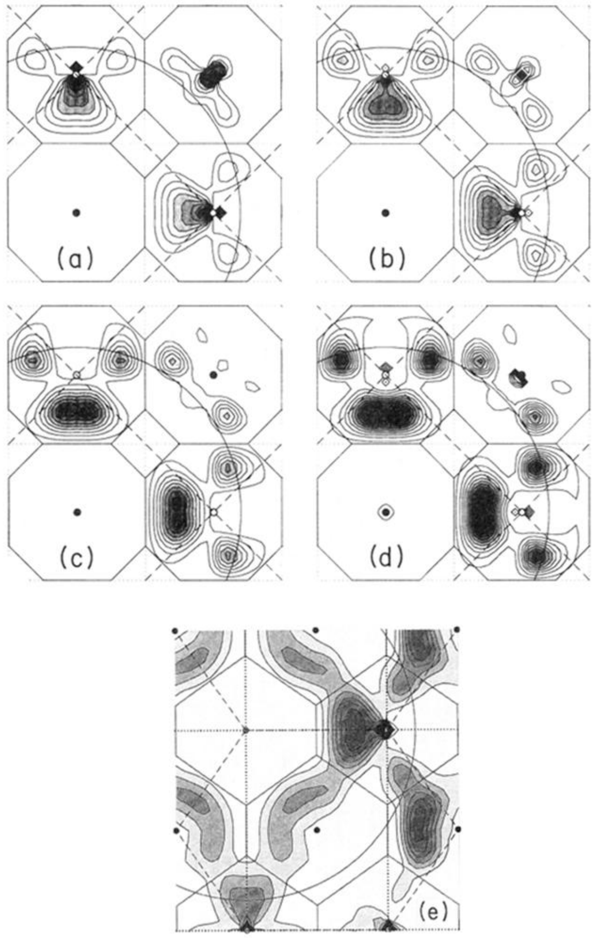

FIG. 13. Diffuse scattering intensities for $Fe_{1-x}O$ as calculated by a Kanzaki model approach to the long-range displacement fields of the 4:1 defect cluster, whose next two cation shells are fully occupied, while the mean lattice was taken as the reference. Results for the (100) plane at (a) $x = 0.054$, (b) $x = 0.08$, (c) $x = 0.104$, (d) $x = 0.13$, and (e) for the (110) plane at $x = 0.08$. (Contours and Brillouin zones as in Fig. 12.)